

Characterisation of a nano-g accelerometer

Claudia Heidemann, Electrical Engineering (IDS), University of Twente, The Netherlands
BSc. committee: Remco Sanders, Boris Boom, Remco Wiegerink, Anne-Johan Annema

Abstract—In this paper, a nano-g accelerometer is characterised by detecting its resonance frequencies in all six degrees of freedom and examining the curvature of comb beams and the proofmass. Furthermore, the needed power to compress all the springs for each step and the weight of the proofmass is measured. It was also found that the proofmass is not in-plane with the rest of the device and gets easily stuck because of oversized stoppers. These results can be used to compare the fabrication results with the intended design and theoretical calculations. Consequently, this will help to improve the next design and make it more reliable in its operation in a seismic network.

Index Terms—MEMS, nano-g, accelerometer, stiction, resonance frequency, topography, SEM, vibrometer, electro-thermal actuation

I. INTRODUCTION

Seismic motion is a constant noise source, which is present everywhere in the world. Unless there are extreme outbursts of seismic motion, for example in form of earthquakes, we as humans do not really notice this noise source. However, when trying to detect gravitational waves, seismic motion will cause fluctuations in the local gravitational field and couple to the test masses of interferometric gravitational wave detectors, such as Virgo (Italy) and LIGO (USA). [1] This noise is called Newtonian noise, which unfortunately cannot be shielded. However, it is possible to measure the seismic activity around the detector and subtract it from the detector output. [2] [3]

For this purpose, the Dutch research institute Nikhef based in Amsterdam, is working on an array of ultra-sensitive MEMS accelerometers. The working principle of these devices is explained in Sec. I-A.

A. Layout and working principle

In Fig. 2 and 1, a schematical overview of the nano-g accelerometer as well as of its cross-section can be found.

The nano-g accelerometer consists of the proofmass in the middle, four actuating combs (CombA1-CombA4) on top and bottom, four sensing combs (Vdrive1-Vdrive4) on left and right, four anti-springs attached to the four corners of the mass and to a shuttle pre-loading mechanism for the compression of these springs. Each pre-loading mechanism is driven by an electro-thermal actuator (ETA) (the working principle of the ETA will be explained in Sec. III-D).

The proofmass has six degrees of freedom for moving. There are three translational movements, namely in x-, y- and

z-direction, where the y-direction is the sensing mode of the device, and three rotational movements around those three axes, denoted as Tx-, Ty- and Tz-mode. In each of the six degrees of freedom, the vibrating mass has a highest movement amplitude. This vibration occurs at a specific frequency, called the resonance frequency, which is given in Eq. 1 with k_{tot} being the total spring constant of all four springs and m being the weigh of the proofmass.

$$f_{res} = \frac{1}{2\pi} \sqrt{k_{tot}/m} \quad (1)$$

This resonance frequency f_{res} can be lowered by decreasing the spring constant k by 5 times under full compression of the springs. As a result, the sensitivity of the nano-g accelerometer increases by a factor 25 for lower frequencies, so that more seismic motion can be recognised. [4]

When applying a (differential) voltage on the top and bottom combs, the comb fingers of the proofmass have an alternating pull force, depending on the amount of charge on each side of the comb pairs. This makes the mass move in the actuated direction.

These devices have also not yet been fully characterised and tested, such that different setups and measurements will be used in order to examine the characteristics of this device, namely the weight of the proofmass, thickness of the device layer (and hence height of the springs), curvature of beams and the proofmass, the process of compressing the springs, in- and out-of-plane movements with its resonance frequencies and the stiction behaviour of the proofmass.

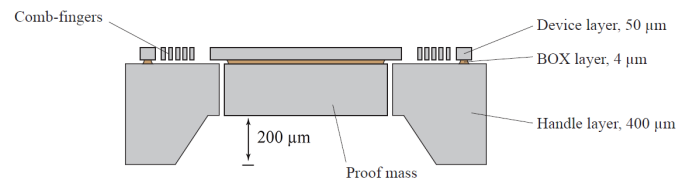


Fig. 1: Schematical cross-section of the nano-g accelerometer. [5]

II. ANALYSIS OF THE SPRING CONSTANTS AND RESONANCE FREQUENCIES

In order to calculate the resonance frequencies for the different modes, it is necessary to calculate the spring constant

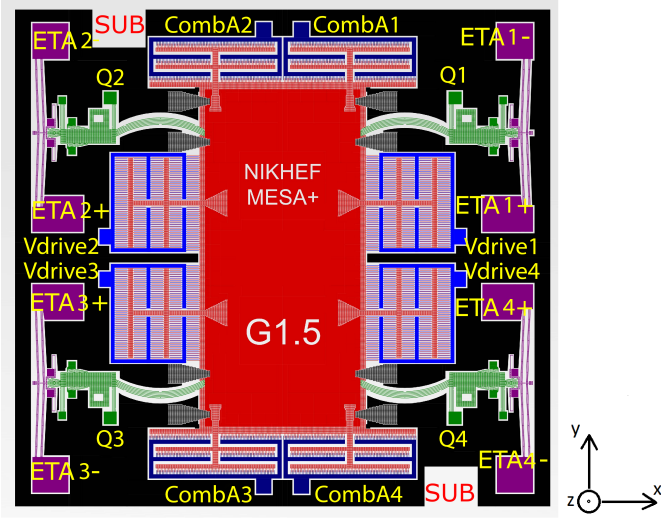


Fig. 2: Pinout and general schematic of the nano-g accelerometer. [3]

for every setup. The springs in this chip consist of four cantilever beams in parallel that are fixed on both sides (on one side to the shuttle pre-loading mechanism, on the other to the proofmass). When the proofmass vibrates in the y -, z - and Tx-mode, the attached cantilever beams as springs will ideally experience only bending without compression or elongation of the springs. For such a case, the general equation of the spring constant in y - and z - direction (translational modes) according to [6] is given in Eq. 2 and 3 where E is the Young's modulus of the beam material (in this case of silicon), I is the second moment of area of the beam and L is the length of the beam. The second moment of area is given in Eq. 4 and 5 where b is the width and h the height of the cantilever beam. Depending on the direction of bending, the values for width and height can be interchanged.

$$k_y = \frac{12EI_y}{L_y^3} \quad (2) \quad k_z = \frac{12EI_z}{L_z^3} \quad (3)$$

$$I_y = \frac{b_y h_y^3}{12} \quad (4) \quad I_z = \frac{b_z h_z^3}{12} \quad (5)$$

After calculating the spring constant for one cantilever beam, one can immediately calculate the spring constant of one spring at each corner by multiplying by four since the four cantilever beams in parallel form one spring. All four springs again are in parallel and therefore, the spring constant of the whole system can be calculated easily as shown in Eq. 6.

$$k_{tot} = 4k_{spring} = 4 \cdot 4k_{beam} \quad (6)$$

In the rotational Tx-mode, the springs are now behaving as torsion springs. Then, the resonance frequency is given by Eq. 7 where k_θ is the torsion spring constant of one spring (not beam) and J is the moment of inertia.

$$f_{res,Tx} = \frac{1}{2\pi} \sqrt{\frac{4k_\theta}{J}} \quad (7)$$

The moment of inertia is given by Eq. 8 according to [7] for a rod rotating around a central axis where m is the total weight of the proofmass and r is half of the proofmass length in y -direction, being the radius of rotation. [7] [8]

$$J = \frac{1}{12} mL^2 = \frac{1}{12} m(2r)^2 = \frac{1}{3} mr^2 \quad (8)$$

Combining the torque equation with Hooke's law, k in Tx-direction can be found in Eq. 9.

$$k_\theta = k_z r^2 \quad (9)$$

The used parameters for the calculated resonance frequencies in Tab. II and III can be found in Tab. I.

As mentioned before, the resonance frequency can be decreased by compressing the springs, which means that the spring constant will decrease as well. In order to calculate the new spring constant k_y in y -direction, the equation must be adapted according to [6], which is shown in Eq. 10. k_z is the spring constant from Eq. 3 in z -direction and r is the same as in Eq. 8.

$$k_{y,1} = k_{y,0} - \frac{F_x}{L_{y,0}} \quad (10)$$

Here, $k_{y,0}$ is the old spring constant from Eq. 2, F_x is the force needed to compress the springs in x -direction to one compression step (by $15 \mu\text{m}$) and $L_{y,0}$ is the new length of the spring that is decreased by $15 \mu\text{m}$. The calculated resonance frequency in y -direction for a compression of springs by $15 \mu\text{m}$ is therefore 137.84 Hz for a device layer thickness of $50 \mu\text{m}$ and 127.86 Hz for $46 \mu\text{m}$, respectively.

TABLE I: Needed parameters for calculating the spring constants and thus the resonance frequencies in Tab. II and III.

Name	Symbol	Value	Unit
Young's modulus (Si)	E	169	GPa
Weight of mass	m	12.7	mg
Force in x-direction	F_x	0.75	mN
Spring height (y)	h_y	8.5	μm
Spring height (z)	h_z	46 [50]	μm
Spring width (y)	b_y	46 [50]	μm
Spring height (z)	b_z	8.5	μm
Spring length (y,0)	$L_{y,0}$	1710	μm
Spring length (y,1)	$L_{y,1}$	1695	μm
Spring length (z)	L_z	2230	μm

TABLE II: Calculated spring constants for the y -, z - and Tx-mode with a device layer thickness of $50 \mu\text{m}$.

	f_{res}	k_{beam}	k_{spring}	k_{tot}
y	181.99 Hz	1.04 N/m	4.15 N/m	16.61 N/m
z	718.83 Hz	16.19 N/m	64.77 N/m	259.07 N/m
Tx	1254.1 Hz	0.18 mN m	0.73 mN m	2.91 mN m

TABLE III: Calculated spring constants for the y-, z- and Tx-mode with a device layer thickness of 46 μm .

	f_{res}	k_{beam}	k_{spring}	k_{tot}
y	174.56 Hz	0.95 N/m	3.82 N/m	15.28 N/m
z	634.32 Hz	12.61 N/m	50.43 N/m	201.74 N/m
Tx	1098.7 Hz	0.18 mN/m	0.57 mN/m	2.26 mN/m

For the x-, Ty- and Tz-mode, the cantilever beams experience more than ideal bending, namely torsion and compression/elongation. This requires different calculations which are not part of this paper.

III. MEASUREMENT SETUPS AND RESULTS

For the characterisation of the nano-g accelerometer, multiple devices had to be used. A complete overview of the used devices can be found in the appendix.

A. Measuring the in- and out-of-plane resonance frequencies

The vibrations of the proofmass in the device can be measured with a Polytec microsystem analyzer MSA-400. The out-of-plane movements are detected with scanning laser Doppler vibrometry while the in-plane movements are recognised with stroboscopic video microscopy (see [9] for a datasheet and a more detailed working principle). The previously described six modes of the nano-g accelerometer can be divided in out-of-plane (Tx-, Ty- and z-mode), which are measured with the software PSV, and in-plane movements (x-, y- and Tz-mode), which are measured with the software PMA.

Out-of-plane modes are easier to detect with this machine as laser Doppler vibrometry is more sensitive than stroboscopic video microscopy. Also, it is useful to scan the whole proofmass with a grid of scanning points, so that a corresponding animation of the movement can be created with the acquired data.

In-plane modes are more difficult to detect and one needs to zoom into a well-visible spot on the device (inspecting the edge of the moving proofmass next to a fixed part of the substrate). A good location for such kind of measurements is one of the pyramid-like fixed structures as seen in Fig. 12 (on the left image).

Then, all the six modes need to be actuated so that the mass starts vibrating. Fig. 3 shows an overview of how the different combs have to be connected in order to actuate the respective modes.

The y- and Tx-mode share the same actuation method. CombA1 is shorted with CombA2 and provided with a sinusoidal signal of around $20 V_{PP}$ and an additional bias voltage of at least $10 V_{DC}$. The bias voltage is needed so that squared terms after squaring a sine wave are removed and one can see the correct frequency (since the force of pulling is proportional to the voltage squared). [3] This will make the proof mass vibrate in the y-direction (in a lower frequency band) and in the Tx-direction (higher frequency band). Next, the Ty-mode can be actuated by shorting CombA2 and CombA3 as well as CombA1 and CombA4. Thus, the mass will rotate around the

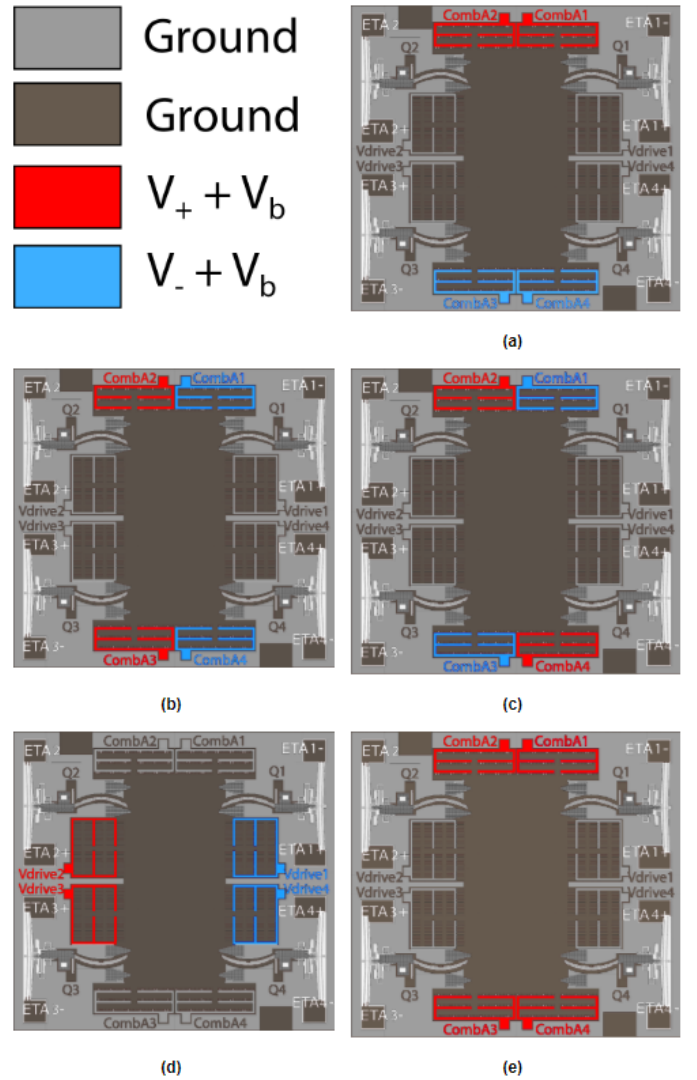


Fig. 3: Actuation of the (a) Tx- and y-mode, (b) Ty-mode, (c) Tz-mode, (d) x-mode and (e) z-mode. Grey and brown represent a ground connection while red and blue are the applied differential voltages (red: $V_+ + V_b$ and blue: $V_- + V_b$).

y-axis. Next, the Tz-mode is actuated similarly to the previous mode by shorting the combs that are diagonal to each other, meaning CombA2 with CombA4 and CombA1 with CombA3, in order to create an in-plane rotation around the z-axis. The x-mode is similar to the y-mode: now the left pair of Vdrive3 and Vdrive4 as well as the right pair of Vdrive1 and Vdrive4 are shorted to make the mass vibrate in x-direction. Finally, the z-mode is actuated by shorting all four actuation combs (CombA1-A4), such that the mass will move up and down (out-of-plane). This mode is the only one that does not require a differential supply voltage.

All the different parts of the chip have bondpads which need to be wirebonded to the pins of a chip carrier. The documentation for this is provided in the appendix. When actuating the different modes, one should ground all other

connections to avoid charge on the different parts of the chip, which could lead to static charge and stiction of the mass.

For these measurements, a handmade shielded measurement box is used (made by Boris Boom [3]), which contains the chip carrier for the nano-g accelerometer on the top. On the backside, there are bigger pins which can be connected to seven BNC connectors for measurements, if needed.

All the measurements were done with a frequency sweep in the expected frequency band (usually a range of around 200 Hz for in-plane and 1000 Hz for out-of-plane measurements) and a supply voltage of $20 V_{PP}$.

The first successful measurements were done in air. Unfortunately, the z-mode could not be detected in air, so that a measurement in a vacuum chamber was needed. The approximate used pressure was between $16 \mu\text{bar}$ – $60 \mu\text{bar}$.

Once a complete dataset for all six modes was successfully obtained, the springs could be compressed by one step. This will be explained further in Sec. III-D. In this compression step, only the y-mode could be successfully detected.

In the process of actuating the various modes, the mass got stuck several times, especially when being in vacuum and after the springs were compressed by one step. Small tapings against the frame of the chip carrier often made the mass get back into the equilibrium position. All the pins then have to be grounded to avoid any kind of charge or pull-in force from one side. However, sometimes a voltage can be applied on the corresponding comb pair, where the proofmass should move to when going back into equilibrium position. For example, when the mass is stuck closer to the bottom comb pair then it sometimes helps to apply a voltage on the top comb pair so that the proofmass gets pulled in the equilibrium direction. Nevertheless, if that does not work it is better to ground every single connection and then tap the frame.

The complete overview of results can be found in the attachment (raw data), in Tab. IV and in Fig. 4. The top figure shows the measured magnitude versus frequency. There are six different data sets for the corresponding modes that show a distinct peak at a certain frequency – the obtained resonance frequency. The bottom figure is the corresponding phase plot where a phase shift of 180° is visible at the resonance frequencies. It can be seen that the data of the y-mode is much clearer than that of the other modes since it is also the main sensing mode of the accelerometer.

TABLE IV: Measured resonance frequencies of all six modes in different setups (in air and in vacuum).

Mode	In air			In vacuum		
	f_{res} [Hz]	Q	P [mbar]	f_{res} [Hz]	Q	P [mbar]
x	719.1	15.12	1000	N/A	N/A	N/A
y	175.47	5.2	1000	N/A	N/A	N/A
z	N/A	N/A	1000	675.95	374.67	0.04
Tx	926.99	8.91	1000	945.42	1574.8	0.05
Ty	1691.97	8.66	1000	1698.22	1565.56	0.06
Tz	825.95	16.37	1000	879.16	9363.97	0.016

B. Weighing the demounted proofmass of the nano-g accelerometer

TABLE V: Comparison between calculated proofmass and measured sample masses with different intact parts

	Calculated	(a)	(b)	(c)
Mass [mg]	12.3 ± 0.5	12.3	11.3	11.4

In case the chips were irreversibly stuck, which means the proofmass was not moving freely under an actuation of the combs (this will be explained later) their proofmass could be taken out in order to weigh the mass and compare with the calculated value from the mask layout in the software CleWin (with the help of the integrated calculator). Demounting the mass was done by removing the whole chip from the PCB (where it was initially glued on) and gently pushing the mass out from the back of the chip (from the side of the cavity, see Tab. 1 for the $200 \mu\text{m}$ space below the proofmass). This mass can then be lifted by using adhesive tip applicators and put on a very sensitive scale. Three masses in different conditions (with missing combs and springs) were measured (shown in Fig. 5) and compared with the theoretical results in Tab. V. The tolerances of the different SOI layers were taken into account. [5] As seen from the almost complete proofmass in Fig 5(a), the calculated value from the mask matches with the measured one.

C. Topography measurements with the white-light interferometer

After the first three devices did not show any expected movement at the supply voltages, topography measurements were carried out. An assumption was that the bottom of the proofmass was stuck to the substrate and therefore not in the same plane as the rest of the chip.

The topography measurements can be done by mounting an objective lens suitable for white-light interferometry onto the vibrometer microscope. In the software package TMS [9], the image had to be adjusted in such a way that circular interferences were visible on the screen. Then, after the scanning procedure, the fixed substrate parts were marked as a reference and the topography of the proofmass with its combs could be measured. With the help of profile lines, it is possible to see the profile of the device in z-direction.

For the first device, it was indeed the case that the device was (at least on one side) touching the substrate beneath it, as the height difference between the combs of the proofmass and the fixed combs was $4 \mu\text{m}$, which is exactly the maximum free moving distance of the proofmass in z-direction (thickness of the BOX-layer, see Fig. 1).

For the other two, including a separate mass from another batch, the scanning area was increased to see a bigger picture of the chip. In all scans, a curvature in the beams and combs could be detected which are showed hereafter.

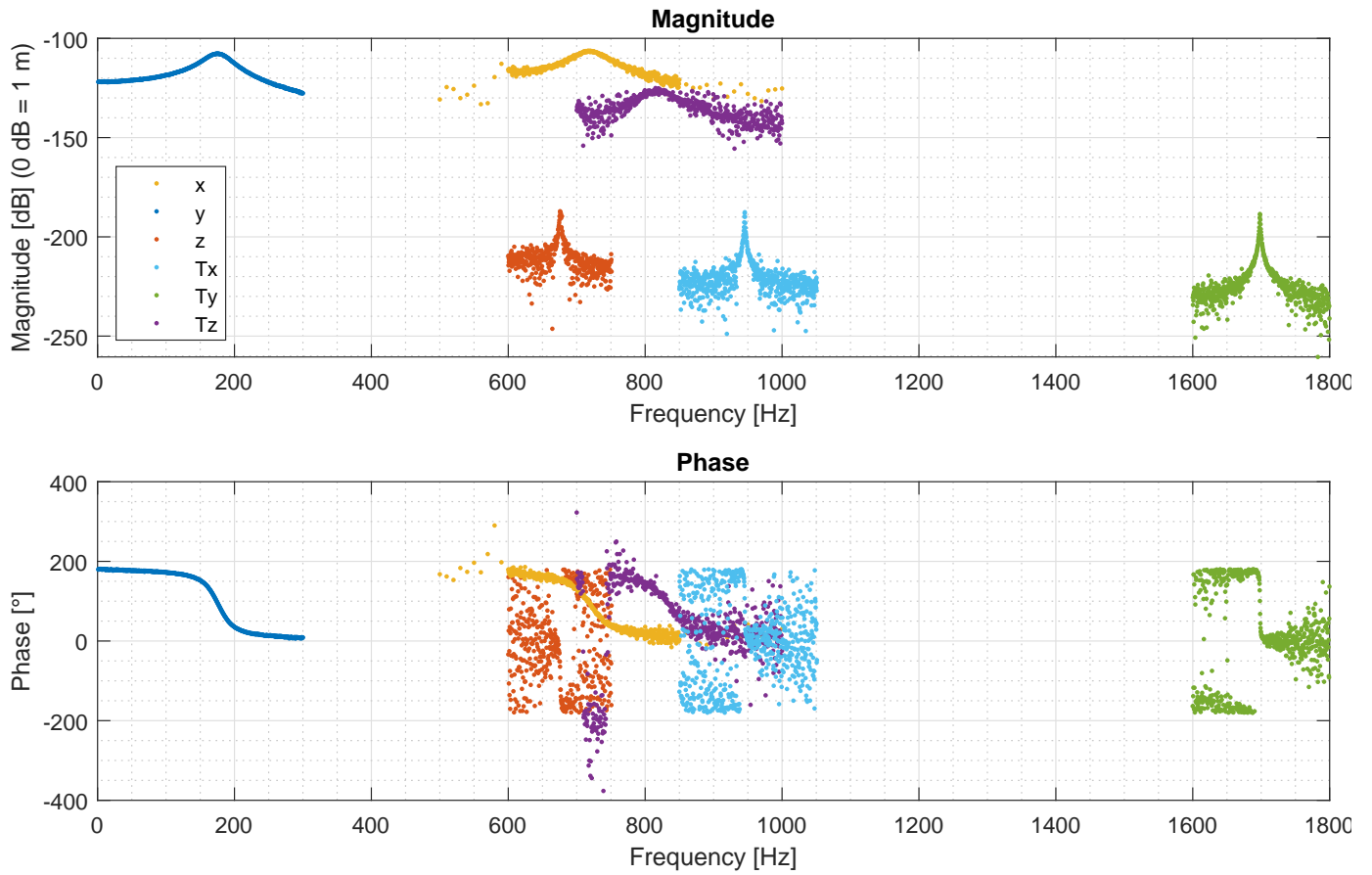


Fig. 4: Measured magnitude and phase of the resonance frequencies for the six modes.

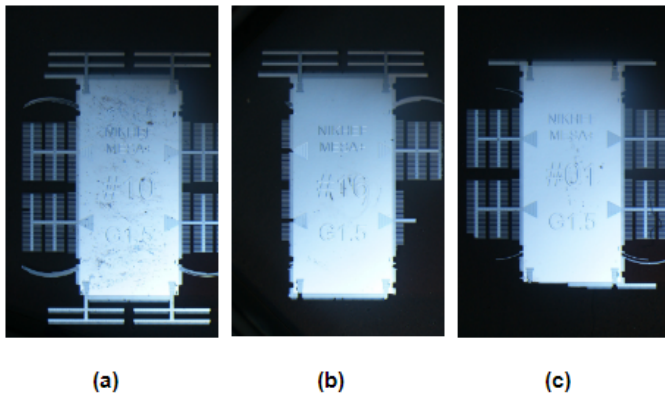


Fig. 5: (a) Almost complete proofmass with one spring missing; (b) Proofmass with Vdrive2-Vdrive4, CombA3-CombA4 and three springs missing; (c) Proofmass with all actuator combs and most of the springs missing.

1) *Curvature of the comb beams*: The curvature of the beams is shown in Fig. 6. The figure shows that in both cases of Vdrive1, the beams were deformed stronger when being part of the chip (while being in an uncompressed state) but are slightly less deformed when being taken out of the device and the proofmass was demounted from the rest of the chip.

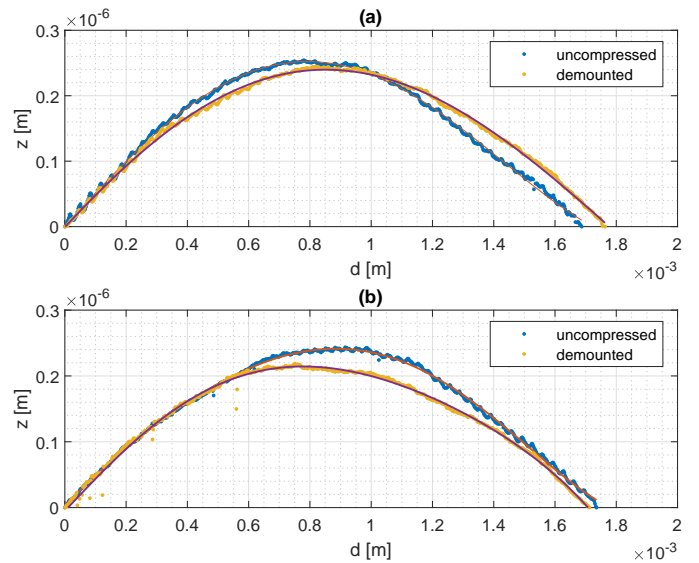


Fig. 6: Curvature of the beam in compressed and demounted state in y-direction: (a) left Vdrive1 comb, (b) right Vdrive1 comb

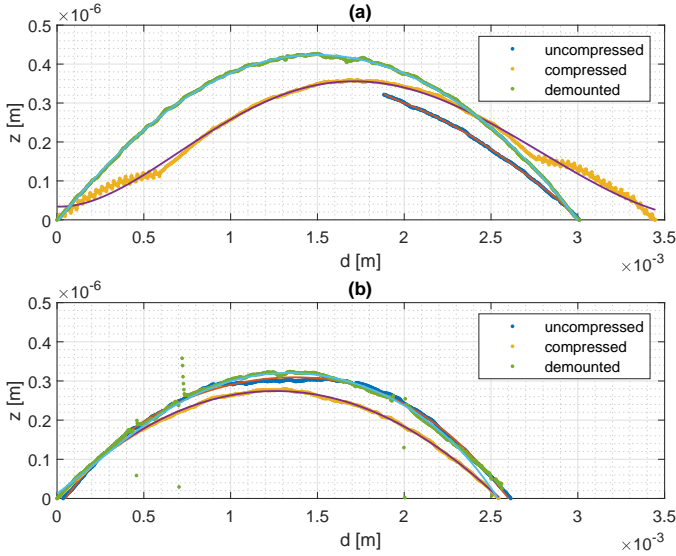


Fig. 7: Curvature of the proofmass in compressed and demounted state: in (a) x-direction and (b) y-direction

2) *Curvature of the proofmass*: The curvature of the proofmass is shown in both directions in Fig. 7. Also here, the demounted state has a slightly smaller curvature. This difference in curvature could be a result of internal stress in the chip causing the proofmass and beams to bent more than outside of the chip where they would be in a relaxed state.

Another feature which is visible in Fig. 7(a) is the non-continuous profile line of the compressed state. This line was taken across the mass where pyramid perforations are on both sides (on the same height as "MESA+" and "G1.5"). Since the perforations belong to the device layer (hence have a thickness of around $50\ \mu\text{m}$), the curvature is different from the proofmass as this one is in total around $254\ \mu\text{m}$ thick.

D. Spring compression by actuation of electro-thermal actuators (ETAs)

Fig. 8 shows the mask layout of an electro-thermal actuator. It consists of two parallel silicon beams and two bond pads on each side. Using these bond pads, a current can be applied through the beam, which heats it up. Due to this heat, the silicon beams expand thermally, mostly in x-direction, so that they can push the shuttle pre-loading mechanism to compress the springs. [6]

For the compression of springs, the ETAs have to be actuated separately at each of the four corners. The chip is fixed on the probe station and all pins, except the two nodes of the respective ETA to be actuated and the nodes of the proofmass (Q1-Q4), are connected to ground. The corresponding two nodes at the ETAs were actuated with a dual-output power supply to avoid voltage on the proofmass. Since the needed voltages were unknown, the supply voltage has been incremented in small steps of $100\ \text{mV}$ while watching the thermal expansion of the ETAs and thus movement of the shuttle system through the microscope of the probe station.

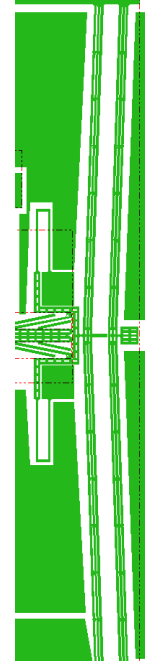


Fig. 8: Mask layout of an electro-thermal actuator.

This movement as well as the corresponding power needed to compress a spring by a certain distance was also recorded and logged, which can be found in the attachment (please check the note in the appendix). Fig. 9 shows the shuttle pre-loading mechanism and Fig. 10(b) displays the needed power for a certain compression distance of the springs in x-direction. For the first compression step, which is with $15\ \mu\text{m}$ the longest of all, the highest power is needed since the beams of the ETAs have to expand most. In Fig. 10(a), it can be seen that in the displayed range of power ($1\ \text{W}$ – $1.4\ \text{W}$ in air), there seems to be a linear relation between the applied power and calculated resistance, which was obtained from the measured power and voltage. However, for other values of power, the linear relation was not examined with this experiment.

E. Measurements with a scanning electron microscope (SEM)

The scanning electron microscope is used to investigate the topography, thickness of beams and stiction behaviour of the proofmass, which cannot be easily seen with a conventional optical microscope. A full overview of the made SEM images can be found in the appendix.

Fig. 11 shows two measurements of a spring cantilever beam. Fig. 11(a) is looking at a 45° angle to measure the spring height and hence thickness of the device layer. The directly measured height must be multiplied with $\sqrt{2}$, so that the measurement angle of 45° is compensated for. The thickness of the device layer is $46\ \mu\text{m}$ which is still within the tolerance of the device layer thickness according to [5]. This is also the reason why Tab. III has been calculated as a comparison. However, the width of one cantilever beam as seen in Fig. 11(b) does not deviate from the measured value in the mask layout (distance measurement tool in CleWin).

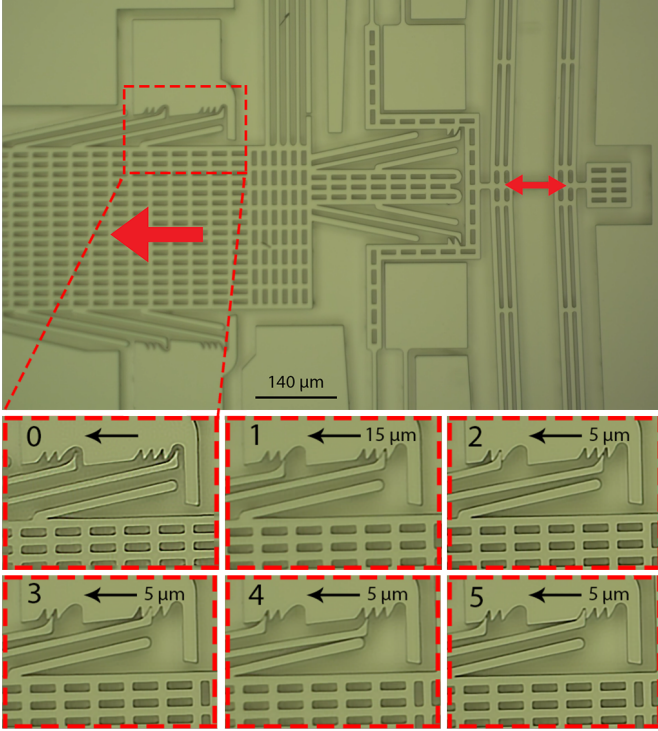


Fig. 9: Top: Overview of the shuttle pre-loading mechanism which can compress the springs by $35\ \mu\text{m}$ in x-direction. Bottom: Six compression steps of the shuttle pre-loading mechanism. [4]

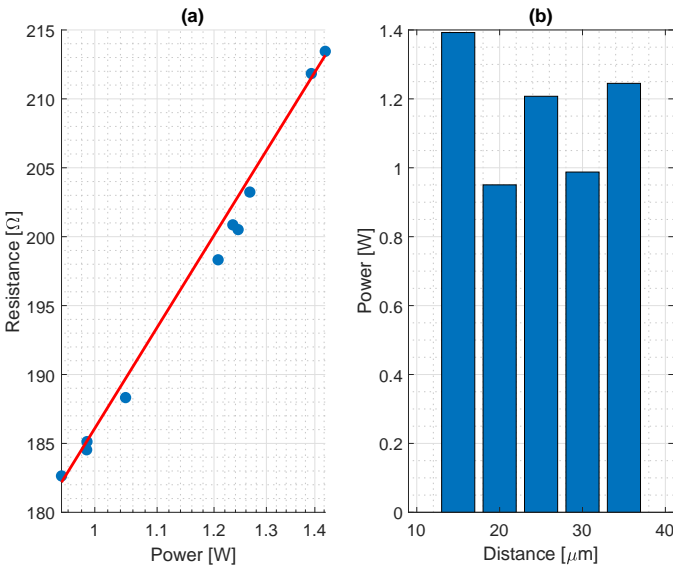


Fig. 10: (a) Measured resistance vs. power with linear regression. (b) Measured power vs. compression distance of the springs.

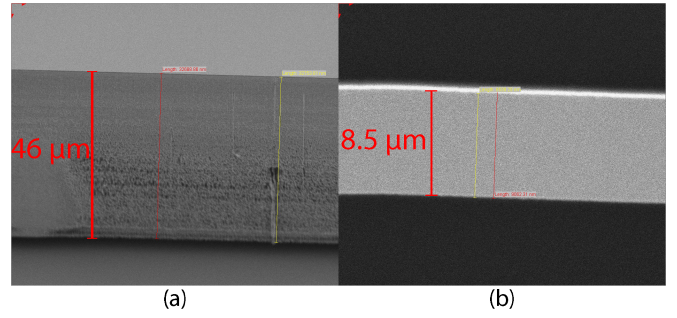


Fig. 11: SEM images of (a) the bottom right spring under a 45° angle. The two measured heights on the right are the direct measurement result under a 45° angle and the value on the left is the actual calculated height taking into account the distortion due to an angle of 45° ; (b) the top right spring with a measurement of its width.

Fig. 12 shows one of the locations where the proofmass touches the fixed substrate and thus gets stuck. Furthermore, there is a noticeable height difference between the proofmass and the substrate. The proofmass appears to be sunk in, which is not yet enough though to touch the substrate beneath the mass. Also here, the directly measured height must be multiplied with $\sqrt{2}$ to compensate for an angle of 45° .

IV. DISCUSSION

In this section, some of the obtained results will be further processed and compared. For example, after calculating and measuring the resonance frequencies, they can be compared with each other and with the provided simulation results from [10]. Fig. 13 shows the comparison of differently obtained resonance frequencies and Fig. 14 compares variously obtained results for resonance frequencies with 0 and $15\ \mu\text{m}$ compression of the springs.

In Fig. 13, one can observe how the measured frequencies are higher than the simulated ones for in-plane movements and lower for out-of-plane movements. This suggests that for out-of-plane modes, the spring constant is lower than expected, which means the springs are less stiff in that direction. This is the opposite for the in-plane motions. Since the actual device layer thickness is lower than expected, this could be a cause for the deviations between simulation and measurement.

This is better illustrated in Fig. 14. It shows a comparison between simulation, calculation (with different values of the thickness) and measurements of the y-mode with no 1-step-compression. The measurement matches the calculation quite well once the actual thickness is taken into account. It also suggests that the earlier measurement was performed with a device having its device layer thickness close to the ideal value of $50\ \mu\text{m}$.

Additionally, the radius of curvature has been calculated for the different comb beams and mass conditions. The radius of curvature ranges from quite small radii for the comb beams ($1.4\ \text{m}$ – $1.7\ \text{m}$) to bigger radii for the mass ($2.6\ \text{m}$ – $4.2\ \text{m}$).

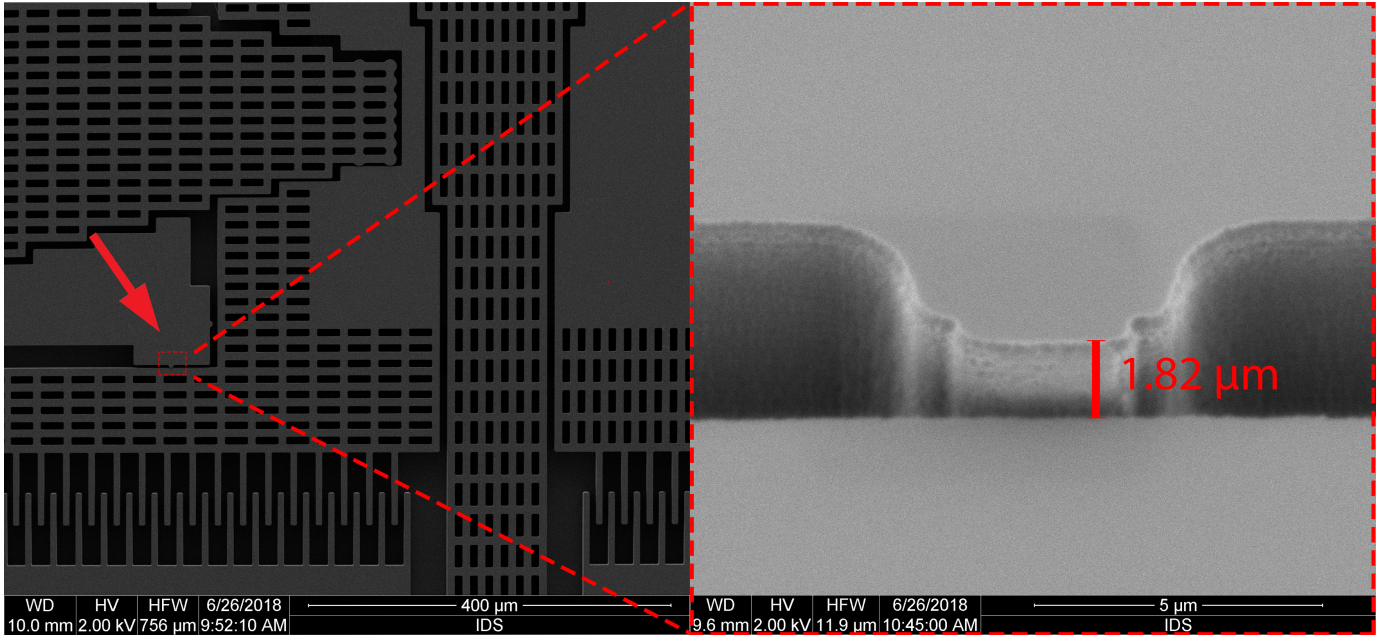


Fig. 12: SEM image of the bottom left stopper touching the proofmass (which is also lower in z-direction than the rest of the device). Left: Overview of the bottom left corner of the mass. On the top, the fixed pyramid-like structure is seen where the gaps between the structure itself and the proofmass are not equal, thus the mass is not in an equilibrium position. Right: Zoomed-in image under a 45° angle where the height difference between the mass and the fixed structure is clearly visible.

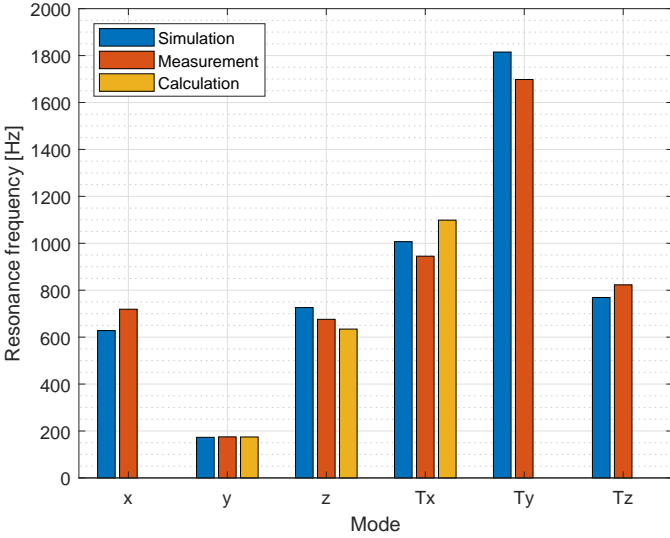


Fig. 13: Comparison between simulation, measurement and calculation of f_{res} [10] [3].

According to [5], a typical radius of curvature of the G5-SOI1-wafer is 8.2 m, which is even higher. This suggests that there is indeed internal stress in the chip that deforms the mass and beams.

Finally, the stopper in Fig. 12 is bigger than expected and that is why the proofmass cannot have the intended space for movements. Also, the whole proofmass appears to be sunk in. However, this is not yet enough to touch the substrate with

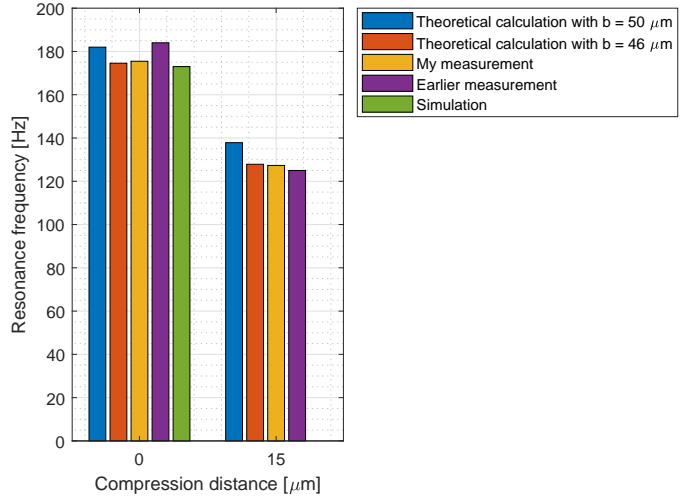


Fig. 14: Comparison of obtained f_{res} in y-direction between two theoretical calculations and two measurements. The values from the red bars were calculated with the use of Fig. 20 in [6] where k_y is given and the earlier measurement (purple bars) refers to Tab. 1 and Fig. 6 in [4].

the proofmass.

V. CONCLUSION & RECOMMENDATIONS

Throughout the experiments, different chips were used as most of them stopped working due to various reasons. Therefore, the measurements of all resonance frequencies without compression of the springs could not be carried out with just

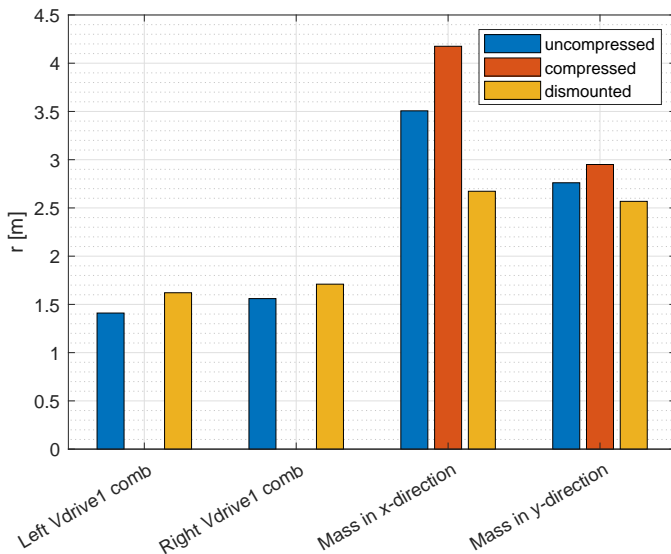


Fig. 15: Comparison of curvature radii between uncompressed, compressed and dismantled state (if applicable) [8].

one device. These frequencies might differ from device to device as it was not checked if the x-mode, for example, occurs at the same frequency as on another measured device. It would be more beneficial, if all resonance frequencies could be measured with one device only (and later also with the stepwise compression of the springs) and then compared with the same measurements of another device to see any possible differences.

The curve fit function of the vibrometer software is imprecise. Having various similar curve fits results in quite different maximum frequencies and Q-factors. Thus, it is recommendable to export the data and process them in Matlab, for example.

Measurements with the SEM showed that the stopper of the bottom and top of the proofmass turned out to be bigger than designed in the mask layout. This leads to an easier stiction of the mass to the fixed edges where it cannot be easily freed. These stoppers can either be designed to be even smaller in size or the etching process needs to be improved.

In general, it is recommended to check the thickness of the device layer after a chip has been fabricated before doing any calculations about the resonance frequencies. Even though the thickness was still within the tolerance of the substrate properties, the weight, spring constants and thus the resonance frequencies changed. If the actual thickness of the device layer (ideally also of the hanging proofmass in the handle layer, though this is not easily achievable) is measured for each device then more precise calculations on the resonance frequencies and dimensions can be done.

Also, the spring constants could be calculated quite precisely for the y-mode. However, as the base of the spring beams is compliant with the cantilever beams themselves, the total length of a spring becomes much longer. A good examination is needed to estimate how much and at which

point exactly the base of the springs starts bending as well. Then, a much better calculated value for k_z can be achieved (which is also needed to calculate T_x). The other modes, like x-, Ty- and Tz-modes, need to be calculated as well. This involves the calculation of spring constants for deforming and/or bending cantilever beams, which is more complicated.

Furthermore, the heavy vacuum chamber should be easier to move. In vacuum, the proofmass is even more sensitive and when pushing the chamber under vacuum, the mass can get stuck or damaged much easier. It would be useful to have an xyz-table (or thin plate since a table would be too high for the vacuum chamber to fit under the lens of the vibrometer) placed under the chamber, so that it can be moved precisely when locating different parts of the device for in- and out-of-plane measurements.

Overall, the device could be characterised well enough to improve it in the future. Also, the detection of all resonance frequencies without compression of the springs will give a guidance on where the resonance frequencies will be located for the full compression of springs. It was also shown that the calculation matched reality quite well once the actual dimensions of the chip were taken into account. The examination of the stiction point of the mass can contribute to a better follow-up design.

ACKNOWLEDGMENTS

I would like to thank especially Remco "Pino" Sanders who helped me with all the different machines, equipment and setups. Thanks also to my supervisors Boris Boom, with whom I had the biggest email conversation in my life so far, and Remco Wiegerink, who was always ready to help spontaneously. Furthermore, thanks to Thomas Schut for helping me with the wirebonder to test first sample devices and Henk-Willem Veltkamp for carrying out white-light interferometer measurements with the device in the cleanroom.

REFERENCES

- [1] LIGO. Gravitational waves from a binary black hole merger observed by LIGO and Virgo. <https://www.ligo.caltech.edu/news/ligo20170927>.
- [2] S. Braccini M. Beccaria, M. Bernardini et al. Relevance of Newtonian seismic noise for the VIRGO interferometer sensitivity. In *Class. Quantum Grav.*, volume 15, pages 3339–3362, 1998. <https://www.nikhef.nl/~jo/virgo/gw/NN/NewtonianNoiseVirgo.pdf>.
- [3] B. Boom. Private communication via email, 2018.
- [4] B. A. Boom, A. Bertolini, E. Hennes, R. A. Brookhuis, R. J. Wiegerink, J. F. J. van den Brand, M. G. Beker, A. Oner, and D. van Wees. Nano-G accelerometer using geometric anti-springs. In *2017 IEEE 30th International Conference on Micro Electro Mechanical Systems (MEMS)*, pages 33–36, Jan 2017.
- [5] A. Bertolini, B. Boom, R. Brookhuis, E. Hennes, and R. Wiegerink. Big mass accelerometer - G5. Process document and fabrication results, Feb 2016.
- [6] J. Kamer. Characterizing the electrical and mechanical behaviour of the Electro-Thermal Actuators of the Nikhef accelerometer MEMS design, Jul 2017.
- [7] M.C. Elwenspoek, G.J.M. Krijnen, R.J. Wiegerink, and T.S.J. Lammerink. *Introduction to Mechanics and Transducer Science*. Sep 2011.
- [8] R. Wiegerink. Private communication in person, 2018.
- [9] Polytec. *MSA-400 Micro System Analyzer*. http://www.ects.pl/files/uploader/Producenci/Polytec/Wibrometry_do_pomiarow_mikrostruktur/MSA-500/LM_BR_MSA-400.pdf.
- [10] E. Hennes. Latest G4./G5 FEM sag and modal analysis. Private communication via email, 2018.

APPENDIX A
MEASUREMENT SETUP MATERIAL

A. List of used measurement equipment

TABLE VI: List of used measurement equipment

Description	Brand and Model	Manual
Waveform generator	Agilent 33220A	http://ecelabs.njit.edu/student_resources/33220_user_guide.pdf
Voltage supply	Delta Elektronika ES-150	http://www.schulz-electronic.de/out/media/ES150_B_E.pdf
Amplifier, 8-channel HV	ESyLAB LM3325	N/A
Dual-channel filter	Stanford Research Systems SR640	http://www.thinksrs.com/downloads/pdfs/manuals/SR640m.pdf
Vibrometer	Polytec MSA-400	http://www.ects.pl/files/uploader/Producenci/Polytec/Wibrometry_do_pomiarow_mikrostruktur/MSA-500/LM_BR_MSA-400.pdf
Scale	Mettler AT261	https://www.artisanng.com/info/mettler_at261_manual.pdf
SourceMeter	Keithley 2410	http://download.tek.com/manual/2410_902_01B.pdf
Dual power supply	Delta Elektronika E018-0.6D	N/A
Oscilloscope	Tektronix TDS 200	http://www.vyssotski.ch/BasicsOfInstrumentation/Tektronix_TDS200_oscilloscope.pdf
Turbomolecular drag pump	Pfeiffer Vacuum TMU 071 P	https://www.ajvs.com/library/Pfeiffer_Vacuum_TMH_071_P_Manual.pdf
Probe station	SSS MicroTec PM5	http://www.bu.edu/phonics/files/2012/06/PM5.pdf
Wire bonder	Westbond 7430E-7630E	http://www.westbond.com/pdf/b747630e.pdf
Microscope camera	Nikon M380E DS-L2	http://www.nikoninstruments.com/images/stories/support/DS-L2/M380E_DS-L2_Manual_v3.2.pdf

B. List of used chips, software and pinout convention

TABLE VII: List of used nano-g accelerometers^a

Wafer	Chip no.	Condition	Note
SOI-1	16	Disassembled	Device 1 after 1st visit ^b
SOI-1	1	Disassembled	Device 2 after 1st visit
SOI-1	8	Stuck	Device 3 after 1st visit
SOI-1	10	Mass only (disassembled)	Separate mass after 2nd visit ^c
SOI-3	1	Stuck	Device 1 after 2nd visit
SOI-3	3	Stuck	Device 2 after 2nd visit

TABLE VIII: List of used software

Name and Version	Purpose
PMA 2.7	In-plane acquisition
PSV 9.3 Acquisition	Out-of-plane acquisition
PSV 9.3	Out-of-plane presentation of data
Pylon Viewer	Live camera for vibrometer
TMS 3.7	Topography scans with white-light interferometry
Matlab 2018a	Data processing
CleWin 5	Mask measurements and calculations

^aPlease, see the process document [5] for the fabrication of the nano-g accelerometers to see a complete overview of the individual sample inspections.

^bFor "Device # after 1st visit" please check Fig. 20.

^cFor "Device # after 2nd visit" please check Fig. 21.

Measurement box	General convention	Connection
11	1	GND
6	6	ETA1+
4	8	Vdrive1
2	10	Q1
80	16	ETA1-
78	18	ETA5+
76	20	Comb1
74	22	GND
72	24	Comb2
70	26	ETA5-
68	28	ETA2-
62	34	Q2
60	36	Vdrive2
58	38	ETA2+
53	43	GND
48	48	ETA3+
46	50	Vdrive3
44	52	Q3
38	58	ETA3-
34	62	Comb3
32	64	GND
30	66	Comb4
26	70	ETA4-
18	78	Vdrive4
20	76	Q4
16	80	ETA4+

Fig. 16: Pin convention to translate between a different pin convention for the measurement box and the according chip carrier pinout (see Fig. 18 and 19 for the pin layout of the measurement box and packaging).

C. Measurement box and chip carrier pinout [3]

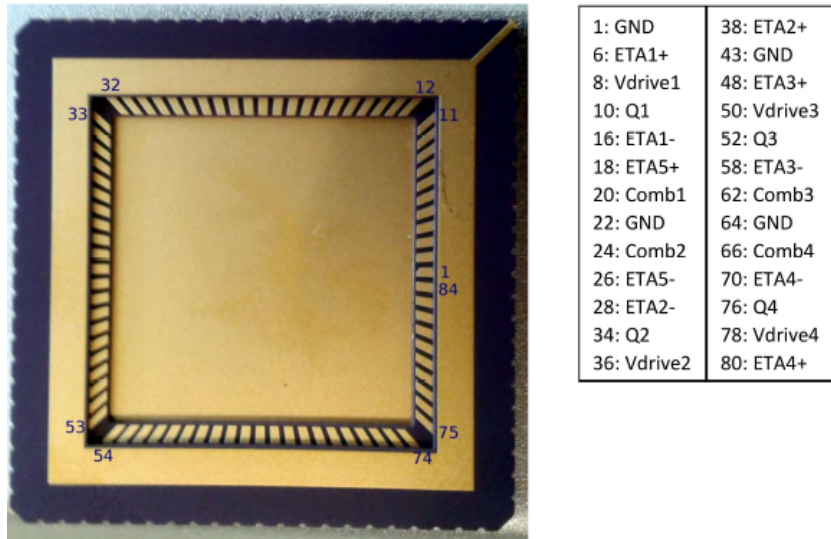


Fig. 17: Standard pinout of chip carriers (which differs from the pinout in the measurement box and that is why Fig. 16 is useful).

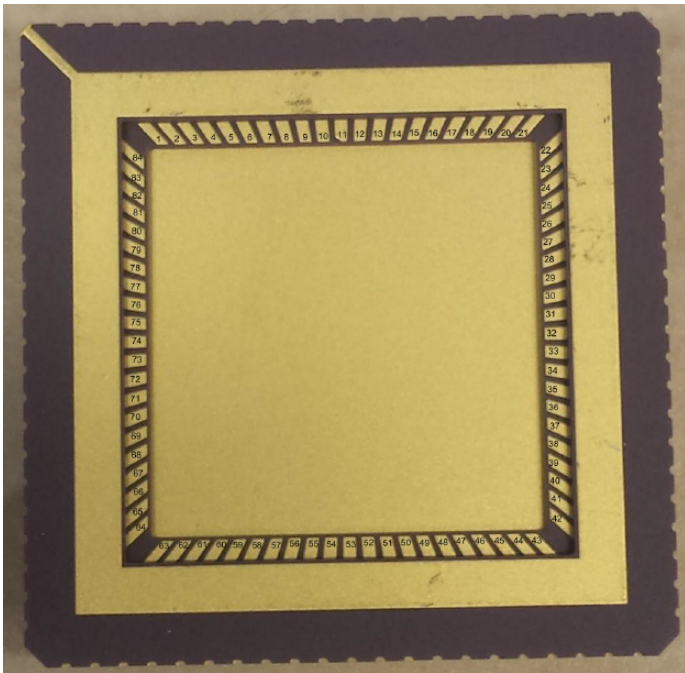


Fig. 18: Pin convention used in the chip carrier of the measurement box.

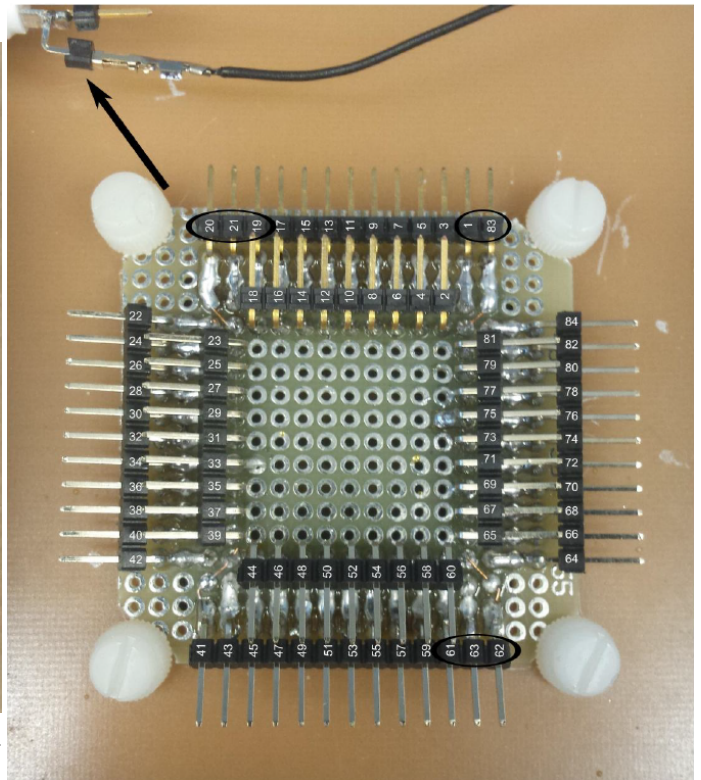


Fig. 19: Pinout of the measurement box.

D. Chip pictures

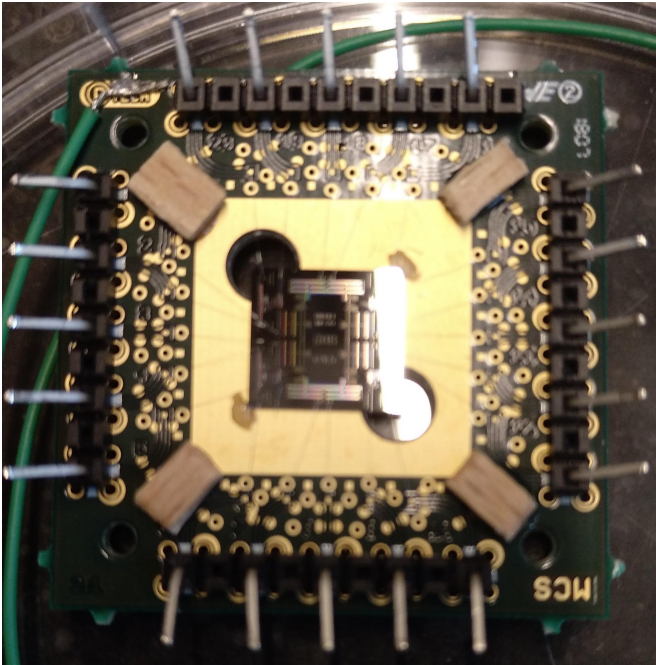


Fig. 20: One of the three devices after the first visit at Nikhef

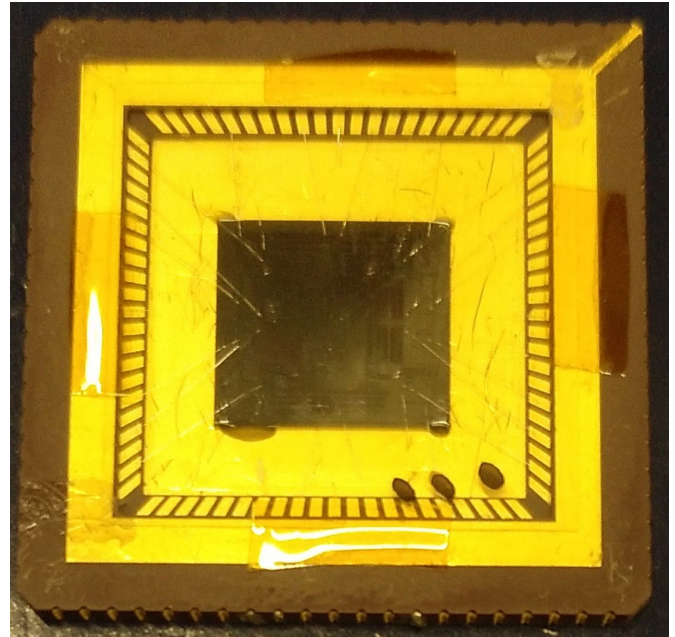


Fig. 21: One of the two devices after the second visit at Nikhef

E. Setup pictures

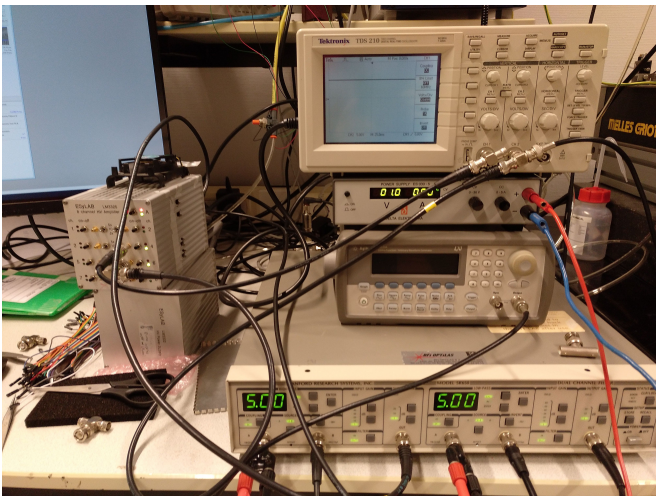


Fig. 22: Basic measurement devices, consisting of an oscilloscope, voltage supply, waveform generator, amplifier and dual-channel filter for differential voltage input.

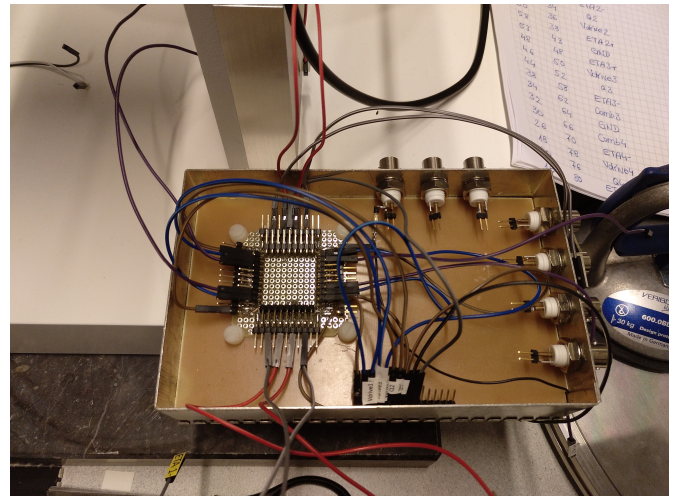


Fig. 23: Made connections inside the measurement box (from chip carrier to BNC connectors on the outside).

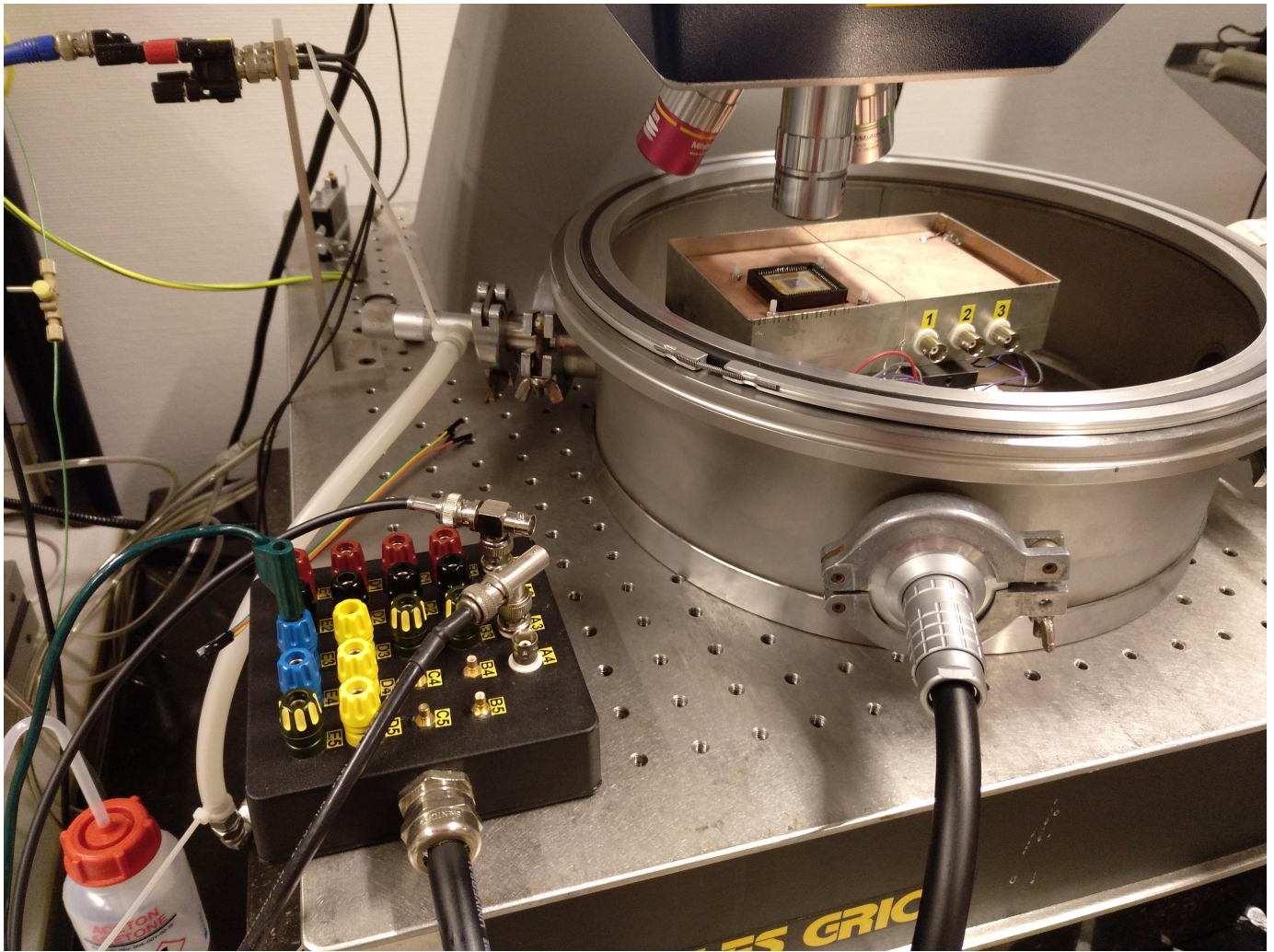


Fig. 24: Measurement box in open vacuum chamber.

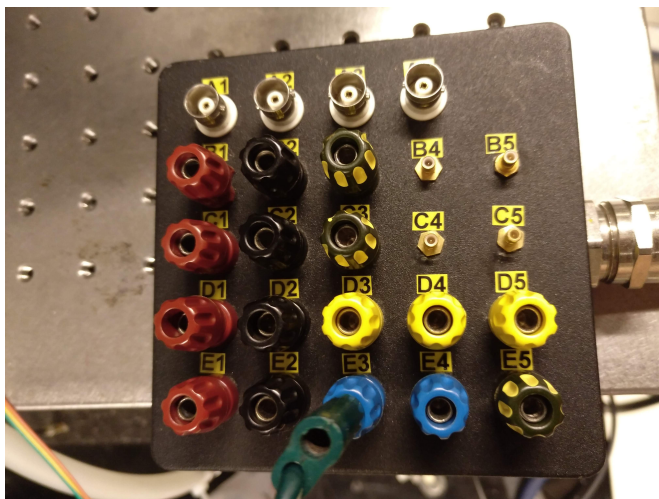


Fig. 25: Pinout of the vacuum chamber outside connections

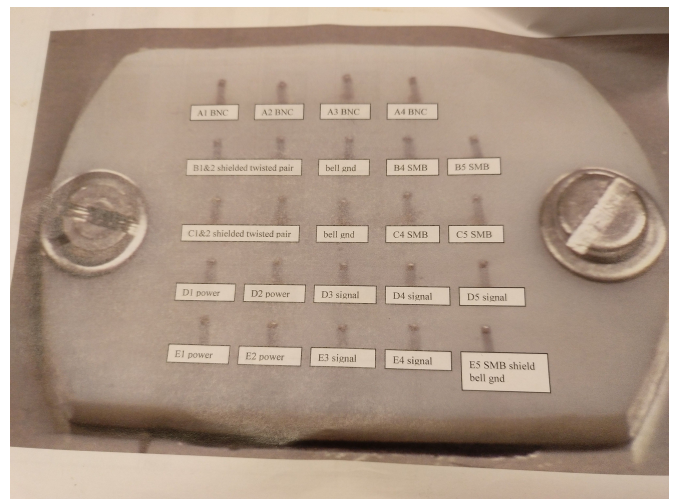
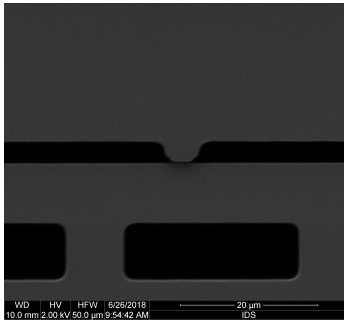
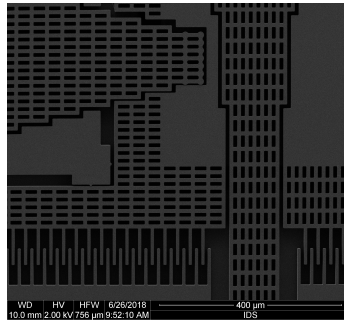


Fig. 26: Pinout of the vacuum chamber inside connections

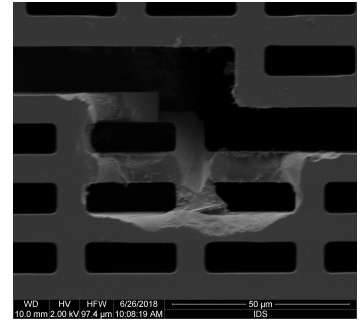
APPENDIX B
SEM IMAGES



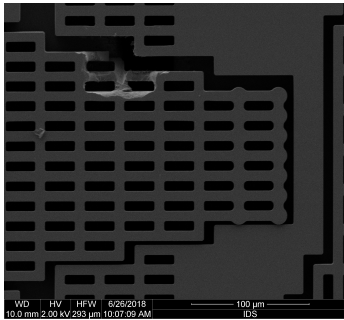
(a) Bottom left stopper.



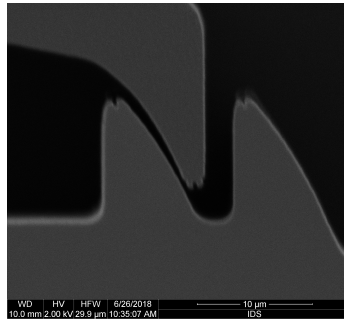
(b) Bottom left overview.



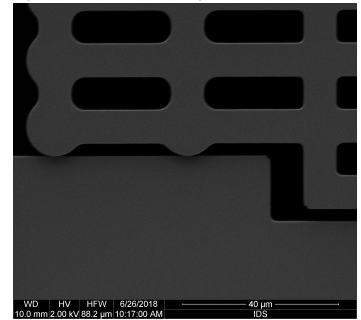
(c) Top left etching structure damaged due to etching mistake.



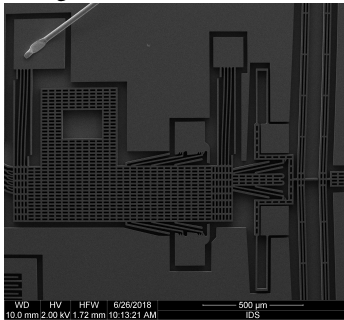
(d) Top left fixed part. Overview of damage.



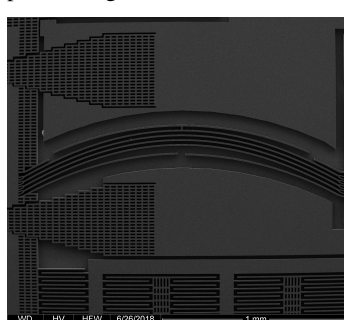
(e) Tooth pair in top right shuttle pre-loading mechanism.



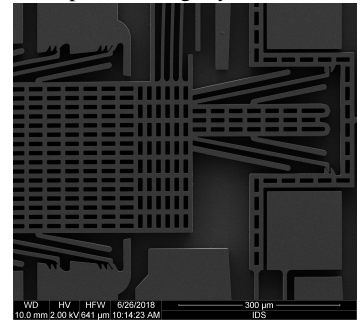
(f) Top right corner. Mass stuck on fixed part and slightly lowered.



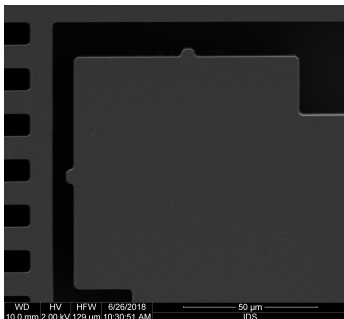
(g) Top right overview of shuttle pre-loading system with ETA actuator on the right.



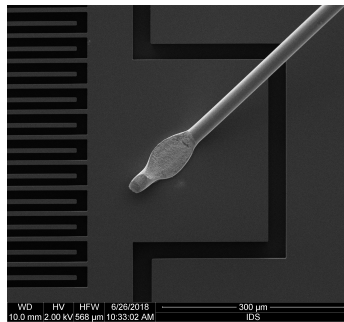
(h) Top right spring compressed with one compression step (15 μm).



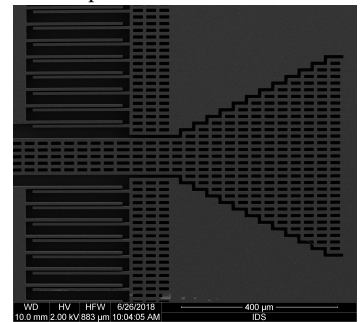
(i) Top right overview of shuttle teeth being all in the first compression step.



(j) Top right stopper.

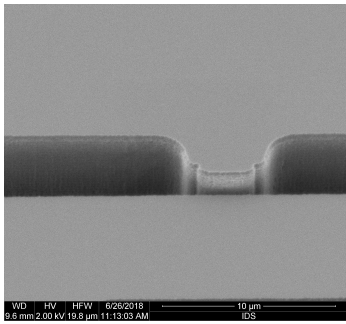


(k) Bondwire connection with Vdrive1.

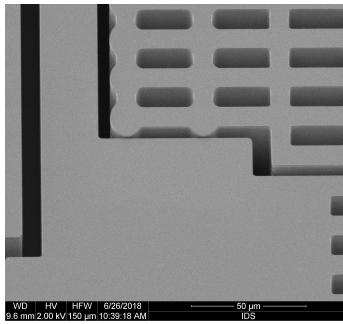


(l) Overview of mass next to Vdrive2.

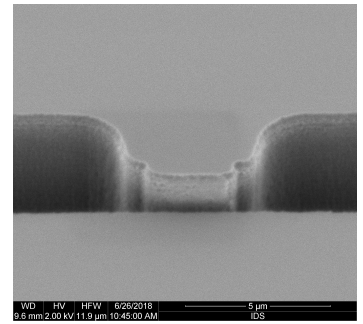
Fig. 27: SEM images taken under an angle of 0°.



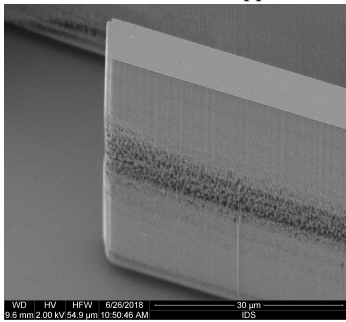
(a) Bottom left stopper.



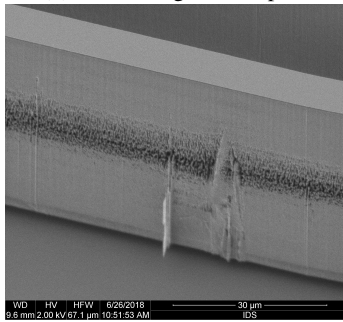
(b) Bottom right fixed part.



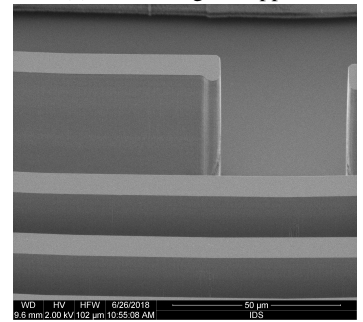
(c) Bottom right stopper.



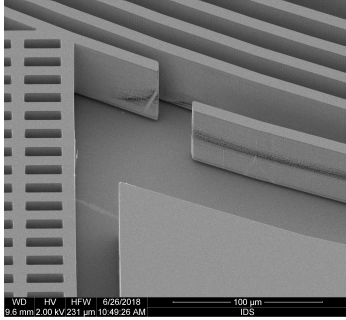
(d) Bottom right spring compressed with one compression step (15 μm).



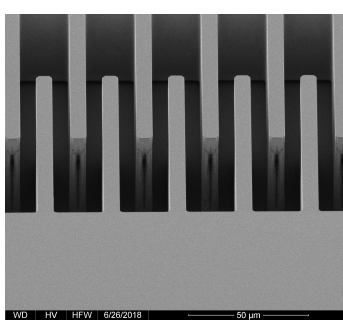
(e) Bottom right spring zoomed in (etching profile 1).



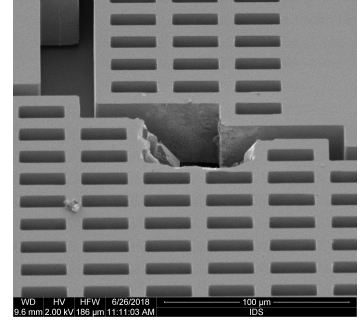
(f) Bottom right spring zoomed in (etching profile 2).



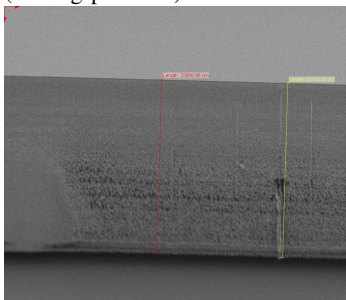
(g) Bottom right spring zoomed in (etching profile 3).



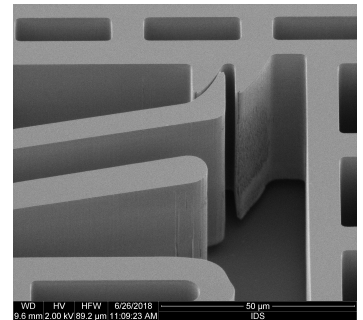
(h) CombA4 etching profile.



(i) Top left etching structure damaged due to etching mistake.



(j) Measurement of the height (under a 45° angle) of the device layer on one of the cantilever beams in the bottom right spring.



(k) Top right tooth of top right shuttle pre-loading mechanism.

Fig. 28: SEM images taken under an angle of 45°.

APPENDIX C
MATLAB CODE FOR GRAPHS AND CALCULATIONS

A. *Weight of proofmass*

```

1 device_layer = 50e-6;           % thickness of device layer [m]
2 device_layer_err = 0.5e-6;
3 BOX_layer = 4e-6;             % thickness of BOX layer [m]
4 BOX_layer_err = 0.2e-6;
5 handle_layer = 400e-6;        % thickness of handle layer [m]
6 handle_layer_err = 10e-6;
7 cavity = 200e-6;             % height of cavity under mass
8 d_Si = 2328;                  % density of Silicon [kg/m^3]
9 d_SiO2 = 2650;                % density of oxide layer [kg/m^3]
10
11 % m_width = 3140e-6;
12 % m_height = 6700e-6;
13 proofmass_area = 19846131.442e-12; % calculated area with the help of CleWin
14 proofmass_thickness_top = device_layer;
15 proofmass_thickness_middle = BOX_layer;
16 proofmass_thickness_bottom = handle_layer-cavity;
17 proofmass_thickness_bottom_err = handle_layer_err-cavity;
18
19 proofmass_device_layer = proofmass_area*device_layer*d_Si;
20 proofmass_device_layer_err = proofmass_area*device_layer_err*d_Si;
21
22 proofmass_BOX_layer = proofmass_area*BOX_layer*d_SiO2;
23 proofmass_BOX_layer_err = proofmass_area*BOX_layer_err*d_SiO2;
24
25 proofmass_handle_layer = proofmass_area*proofmass_thickness_bottom*d_Si;
26 proofmass_handle_layer_err = proofmass_area*handle_layer_err*d_Si;
27
28 proofmass_weight = proofmass_device_layer+proofmass_BOX_layer+proofmass_handle_layer
29 proofmass_weight_err = proofmass_device_layer_err+proofmass_BOX_layer_err+proofmass_handle_layer_err
30
31 % calculated area with the help of CleWin
32
33 Vdrive_area_tot = 2933744.476e-12;
34 Vdrive_weight = Vdrive_area_tot*device_layer*d_Si;
35 Vdrive_weight_err = Vdrive_area_tot*device_layer_err*d_Si;
36
37 Comb_area_tot = 2091960.38e-12;
38 Comb_weight = Comb_area_tot*device_layer*d_Si;
39 Comb_weight_err = Comb_area_tot*device_layer_err*d_Si;
40
41 m_weight = proofmass_weight+Vdrive_weight+Comb_weight
42 Vdrive_comb_err = Vdrive_weight_err+Comb_weight_err

```

B. *Beam curvature*

```

1 % get data
2
3 load 'beam_curvature_data.mat'
4
5 comb_y1_d_0 = 4*uncompressed(:,7);
6 comb_y1_z_0 = uncompressed(:,8);
7 comb_y1_d_0 = rmmissing(comb_y1_d_0); % deleting NaN value of the matrix
8 comb_y1_z_0 = rmmissing(comb_y1_z_0);
9
10 comb_y1_z_0 = comb_y1_z_0+[1.013380000000000e-07]; % shifting graph to origin
11 comb_y1_z_0 = comb_y1_z_0-(2.6080e-04*comb_y1_d_0); % put end point
12
13 comb_y1_d_u = 4*demounted(:,7);
14 comb_y1_z_u = demounted(:,8);
15 comb_y1_d_u = rmmissing(comb_y1_d_u);
16 comb_y1_z_u = rmmissing(comb_y1_z_u);
17
18 comb_y1_z_u = comb_y1_z_u-[8.441900000000000e-08]; % shifting graph to origin
19 comb_y1_z_u = comb_y1_z_u+(1.5322e-04*comb_y1_d_u); % put end point
20

```

```

21 comb_y2_d_0 = 4*uncompressed(:,5);
22 comb_y2_z_0 = uncompressed(:,6);
23 comb_y2_d_0 = rmmissing(comb_y2_d_0);
24 comb_y2_z_0 = rmmissing(comb_y2_z_0);
25
26 comb_y2_z_0 = comb_y2_z_0+[2.854930000000000e-07];           % shifting graph to origin
27 comb_y2_z_0 = comb_y2_z_0+(2.9903e-04*comb_y2_d_0);       % put end point
28
29 comb_y2_d_u = 4*demounted(:,5);
30 comb_y2_z_u = demounted(:,6);
31 comb_y2_d_u = rmmissing(comb_y2_d_u);
32 comb_y2_z_u = rmmissing(comb_y2_z_u);
33
34 comb_y2_z_u = comb_y2_z_u+[3.925010000000000e-07];       % shifting graph to origin
35 comb_y2_z_u = comb_y2_z_u+(1.1098e-04*comb_y2_d_u);     % put end point
36
37 % plot
38
39 figure(1)
40
41 subplot(2,1,1)
42
43 h1 = plot(comb_y1_d_0,comb_y1_z_0, '. ');
44 hold on;
45 fit_y1_0 = polyfit(comb_y1_d_0,comb_y1_z_0,5);           % finding polynomial fit to set of ...
46 val_y1_0 = polyval(fit_y1_0,comb_y1_d_0);
47 plot(comb_y1_d_0,val_y1_0, '-');
48 hold on;
49
50 h2 = plot(comb_y1_d_u,comb_y1_z_u, '. ', 'LineWidth',1);
51 hold on;
52 fit_y1_u = polyfit(comb_y1_d_u,comb_y1_z_u,5);
53 val_y1_u = polyval(fit_y1_u,comb_y1_d_u);
54 plot(comb_y1_d_u,val_y1_u, '- ', 'LineWidth',1);
55 hold on;
56
57 title('(a)');
58 xlabel('d [m]');
59 ylabel('z [m]');
60 ax = gca ;
61 ax.YAxis.Exponent = -6;
62 axis([0 2e-3 0 0.3e-6])
63 legend([h1 h2],{'uncompressed','demounted'});
64 grid on
65 % legend('uncompressed','demounted','Location','south');
66 grid minor
67 %set(gcf,'units','normalized','outerposition',[0 0 0.5 0.5])
68
69
70 subplot(2,1,2)
71
72 h3 = plot(comb_y2_d_0, comb_y2_z_0, '. ');
73 hold on;
74 fit_y2_0 = polyfit(comb_y2_d_0,comb_y2_z_0,5);
75 val_y2_0 = polyval(fit_y2_0,comb_y2_d_0);
76 plot(comb_y2_d_0,val_y2_0, '- ', 'LineWidth',1);
77 hold on;
78
79 h4 = plot(comb_y2_d_u,comb_y2_z_u, '. ');
80 hold on;
81 fit_y2_u = polyfit(comb_y2_d_u,comb_y2_z_u,5);
82 val_y2_u = polyval(fit_y2_u,comb_y2_d_u);
83 plot(comb_y2_d_u,val_y2_u, '- ', 'LineWidth',1);
84 hold off;
85
86 % plot
87
88 title('(b)');
89 xlabel('d [m]');
90 ylabel('z [m]');
91 ax = gca ;
92 ax.YAxis.Exponent = -6;
93 axis([0 2e-3 0 0.3e-6])

```

```

94 legend([h3 h4], {'uncompressed', 'demounted'});
95 grid on
96 grid minor
97 % legend('uncompressed', 'demounted', 'Location', 'south');
98 %set(gcf, 'units', 'normalized', 'outerposition', [0 0 0.5 0.5])
99 print('beam_curvature.eps', '-depsc');
100 % movefile('beam_curvature.eps', 'H:\My Drive\12 Bachelor ...
    assignment\IDS\Paper\Conference-LaTeX-template_5-8-18\Images');
101 movefile('beam_curvature.eps', 'D:\Google Drive\12 Bachelor ...
    assignment\IDS\Paper\Conference-LaTeX-template_5-8-18\Images');

```

C. Mass curvature

```

1 % load data
2
3 load 'mass_curvature_data.mat'
4
5 % uncompressed
6
7 mass_x_d_u = 4*uncompressed(:,3);
8 mass_x_z_u = uncompressed(:,4);
9 mass_x_d_u = rmissing(mass_x_d_u);
10 mass_x_z_u = rmissing(mass_x_z_u);
11
12 mass_x_d_u = mass_x_d_u+[0.00300976225200000-0.00112647245600000];
13 mass_x_z_u = mass_x_z_u-[7.970000000000000e-07];
14
15 mass_y_d_u = 4*uncompressed(:,1);
16 mass_y_d_u = rmissing(mass_y_d_u);
17 mass_y_d_u = mass_y_d_u-[8.304884000000000e-06];
18 mass_y_z_u = uncompressed(:,2);
19 mass_y_z_u = rmissing(mass_y_z_u);
20
21 mass_y_z_u = mass_y_z_u-[3.565100000000000e-07];
22 mass_y_z_u = mass_y_z_u-(2.4661e-04*mass_y_d_u);
23
24 % compressed
25
26 mass_x_d_c = 4*compressed(:,1);
27 mass_x_d_c = rmissing(mass_x_d_c);
28 mass_x_z_c = compressed(:,2);
29 mass_x_z_c = rmissing(mass_x_z_c);
30
31 mass_x_z_c = mass_x_z_c+[3.641900000000000e-08];
32 mass_x_z_c = mass_x_z_c+(2.9409e-05*mass_x_d_c);
33
34 mass_y_d_c = 4*compressed(:,3);
35 mass_y_d_c = rmissing(mass_y_d_c);
36 mass_y_z_c = compressed(:,4);
37 mass_y_z_c = rmissing(mass_y_z_c);
38
39 mass_y_z_c = mass_y_z_c-[3.946300000000000e-08];
40 mass_y_z_c = mass_y_z_c+(4.0515e-05*mass_y_d_c);
41
42
43 % demounted
44
45 mass_x_d_d = 4*demounted(:,1);
46 mass_x_d_d = rmissing(mass_x_d_d);
47 mass_x_z_d = demounted(:,2);
48 mass_x_z_d = rmissing(mass_x_z_d);
49
50 mass_x_z_d = mass_x_z_d+[1.284430000000000e-07];
51 mass_x_z_d = mass_x_z_d+(6.1440e-06*mass_x_d_d);
52
53 mass_y_d_d = 4*demounted(:,3);
54 mass_y_d_d = rmissing(mass_y_d_d);
55 mass_y_z_d = demounted(:,4);
56 mass_y_z_d = rmissing(mass_y_z_d);
57
58 mass_y_z_d = mass_y_z_d+[3.028400000000000e-08];
59

```

```

60
61 figure
62
63 % x-direction
64
65 subplot(2,1,1)
66
67 h1 = plot(mass_x_d_u,mass_x_z_u, '.');
68 hold on;
69     fit_mass_x_u = polyfit(mass_x_d_u,mass_x_z_u,5);           % finding polynomial fit ...
70     to set of data points
71     val_mass_x_u = polyval(fit_mass_x_u,mass_x_d_u);
72     plot(mass_x_d_u,val_mass_x_u, '-', 'LineWidth',1);
73     hold on;
74 h2 = plot(mass_x_d_c,mass_x_z_c, '.');
75 hold on;
76     fit_mass_x_c = polyfit(mass_x_d_c,mass_x_z_c,5);           % finding polynomial fit ...
77     to set of data points
78     val_mass_x_c = polyval(fit_mass_x_c,mass_x_d_c);
79     plot(mass_x_d_c,val_mass_x_c, '-', 'LineWidth',1);
80     hold on;
81 h3 = plot(mass_x_d_d,mass_x_z_d, '.');
82 hold on;
83     fit_mass_x_d = polyfit(mass_x_d_d,mass_x_z_d,5);           % finding polynomial fit ...
84     to set of data points
85     val_mass_x_d = polyval(fit_mass_x_d,mass_x_d_d);
86     plot(mass_x_d_d,val_mass_x_d, '-', 'LineWidth',1);
87     hold on;
88 axis([0 3.5e-3 0 0.5e-6])
89 title('(a)');
90 xlabel('d [m]');
91 ylabel('z [m]');
92 ax = gca ;
93 ax.YAxis.Exponent = -6;
94
95 legend([h1 h2 h3], 'uncompressed', 'compressed', 'demounted', 'location', 'northeast');
96 grid on
97 grid minor
98 %set(gcf, 'units', 'normalized', 'outerposition', [0 0 0.5 0.5])
99
100 % y-direction
101
102 subplot(2,1,2)
103
104 h4 = plot(mass_y_d_u,mass_y_z_u, '.');
105 hold on;
106     fit_mass_y_u = polyfit(mass_y_d_u,mass_y_z_u,5);           % finding polynomial fit ...
107     to set of data points
108     val_mass_y_u = polyval(fit_mass_y_u,mass_y_d_u);
109     plot(mass_y_d_u,val_mass_y_u, '-', 'LineWidth',1);
110     hold on;
111 h5 = plot(mass_y_d_c,mass_y_z_c, '.');
112 hold on;
113     fit_mass_y_c = polyfit(mass_y_d_c,mass_y_z_c,5);           % finding polynomial fit ...
114     to set of data points
115     val_mass_y_c = polyval(fit_mass_y_c,mass_y_d_c);
116     plot(mass_y_d_c,val_mass_y_c, '-', 'LineWidth',1);
117     hold on;
118 h6 = plot(mass_y_d_d,mass_y_z_d, '.');
119 hold on;
120     fit_mass_y_d = polyfit(mass_y_d_d,mass_y_z_d,5);           % finding polynomial fit ...
121     to set of data points
122     val_mass_y_d = polyval(fit_mass_y_d,mass_y_d_d);
123     plot(mass_y_d_d,val_mass_y_d, '-', 'LineWidth',1);
124     hold on;
125 hold off;
126
127 title('(b)');
128 xlabel('d [m]');
129 ylabel('z [m]');
130 axis([0 3.5e-3 0 0.5e-6])
131 legend([h4 h5 h6], 'uncompressed', 'compressed', 'demounted', 'location', 'northeast');
132 grid on
133 grid minor

```

```

128     ax = gca ;
129 ax.YAxis.Exponent = -6;
130     %set(gcf, 'units', 'normalized', 'outerposition', [0 0 0.5 0.5])
131     % print('mass_curvature', '-dpng');
132     print('mass_curvature.eps', '-depsc');
133     % movefile('mass_curvature.eps', 'H:\My Drive\12 Bachelor ...
assignment\IDS\Paper\Conference-Latex-template_5-8-18\Images');
134     movefile('mass_curvature.eps', 'D:\Google Drive\12 Bachelor ...
assignment\IDS\Paper\Conference-Latex-template_5-8-18\Images');

```

D. Calculation of radius of curvature

```

1 % get data of beams
2
3 load 'radius of curvature beams data.mat'
4
5 % get data of mass
6
7 load 'radius of curvature mass data.mat';
8
9 % radius of curvature beams
10
11 defl_mass_x_c = max(val_y1_0);
12 l_y_0 = comb_y1_d_0(end);
13 R_y1_0 = l_y_0^2/(8*defl_mass_x_c);
14
15 defl_y1_u = max(val_y1_u);
16 l_y_u = comb_y1_d_u(end);
17 R_y1_u = l_y_u^2/(8*defl_y1_u);
18
19 defl_y2_0 = max(val_y2_0);
20 l_y_0 = comb_y2_d_0(end);
21 R_y2_0 = l_y_0^2/(8*defl_y2_0);
22
23 defl_y2_u = max(val_y2_u);
24 l_y_u = comb_y2_d_u(end);
25 R_y2_u = l_y_u^2/(8*defl_y2_u);
26
27 % radius of curvature mass
28
29 defl_mass_x_u = max(val_mass_x_u);
30 l_mass_x_u = mass_x_d_u(end);
31 R_mass_x_u = l_mass_x_u^2/(8*defl_mass_x_u);
32
33 defl_mass_x_c = max(val_mass_x_c);
34 l_mass_x_c = mass_x_d_c(end);
35 R_mass_x_c = l_mass_x_c^2/(8*defl_mass_x_c);
36
37 defl_mass_x_d = max(val_mass_x_d);
38 l_mass_x_d = mass_x_d_d(end);
39 R_mass_x_d = l_mass_x_d^2/(8*defl_mass_x_d);
40
41 defl_mass_y_u = max(val_mass_y_u);
42 l_mass_y_u = mass_y_d_u(end);
43 R_mass_y_u = l_mass_y_u^2/(8*defl_mass_y_u);
44
45 defl_mass_y_c = max(val_mass_y_c);
46 l_mass_y_c = mass_y_d_c(end);
47 R_mass_y_c = l_mass_y_c^2/(8*defl_mass_y_c);
48
49 defl_mass_y_d = max(val_mass_y_d);
50 l_mass_y_d = mass_y_d_d(end);
51 R_mass_y_d = l_mass_y_d^2/(8*defl_mass_y_d);
52
53 left_Vdrive1 = [R_y1_0, NaN, R_y1_u];
54 right_Vdrive2 = [R_y2_0, NaN, R_y2_u];
55 mass_x = [R_mass_x_u, R_mass_x_c, R_mass_x_d];
56 mass_y = [R_mass_y_u, R_mass_y_c, R_mass_y_d];
57 data = [left_Vdrive1; right_Vdrive2; mass_x; mass_y];
58
59 figure

```

```

60 x = categorical({'Left Vdrivel comb';'Right Vdrivel comb';'Mass in x-direction';'Mass in ...
    y-direction'});
61 x = reordercats(x,{'Left Vdrivel comb';'Right Vdrivel comb';'Mass in x-direction';'Mass in ...
    y-direction'});
62 bar(x,data)
63 % title('Radius of beam curvature');
64 ylabel('r [m]');
65 legend('uncompressed','compressed','dismounted');
66 grid on
67 grid minor
68 print('curvature_radius.eps','-depsc');
69 % movefile('beam_curvature_radius.eps','H:\My Drive\12 Bachelor ...
    assignment\IDS\Paper\Conference-Latex-template_5-8-18\Images');
70 movefile('curvature_radius.eps','D:\Google Drive\12 Bachelor ...
    assignment\IDS\Paper\Conference-Latex-template_5-8-18\Images');

```

E. ETA actuation

```

1 I = P./V;
2 R = V./I;
3
4 figure
5
6 subplot(1,2,1)
7
8 scatter(P,R,'filled')
9 fit = lsline;
10 fit.LineWidth = 1.5;
11 axis(gca)
12 set(gca,'XScale','log','YScale','linear')
13 fit.Color = 'r';
14 title('(a)')
15 xlabel('Power [W]')
16 ylabel('Resistance [\Omega]')
17 grid on
18 grid minor
19
20 %print('resistance_vs_power','-dpng');
21 %movefile('resistance_vs_power.png','D:\Google Drive\12 Bachelor ...
    assignment\IDS\Paper\Conference-Latex-template_5-8-18\Images');
22
23 hold on;
24
25 subplot(1,2,2)
26 bar(d,P)
27 title('(b)')
28 xlabel('Distance [\mu m]')
29 ylabel('Power [W]')
30 grid on
31 grid minor
32 % print('ETA_actuation','-dpng');
33 %movefile('power_vs_distance.png','D:\Google Drive\12 Bachelor ...
    assignment\IDS\Paper\Conference-Latex-template_5-8-18\Images');
34 print('ETA_actuation.eps','-depsc');
35 movefile('ETA_actuation.eps','H:\My Drive\12 Bachelor ...
    assignment\IDS\Paper\Conference-Latex-template_5-8-18\Images');

```

F. Overview of resonance frequencies

```

1 % all in one plot
2 load 'f_res data.mat'
3
4 x_freq = x(:,1);
5 x_mag = x(:,2);
6 x_phase = x(:,3);
7 y_freq = y(:,1);
8 y_mag = y(:,2);
9 y_phase = y(:,3);
10 z_freq = z(:,1);

```

```

11 z_mag = z(:,2);
12 z_phase = z(:,3);
13 Tx_freq = Tx(:,1);
14 Tx_mag = Tx(:,2);
15 Tx_phase = Tx(:,3);
16 Ty_freq = Ty(:,1);
17 Ty_mag = Ty(:,2);
18 Ty_phase = Ty(:,3);
19 Tz_freq = Tz(:,1);
20 Tz_mag = Tz(:,2);
21 Tz_phase = Tz(:,3);
22
23 figure
24
25 subplot(2,1,1)
26
27
28 h1 = plot(y_freq,y_mag,'.');
29 hold on;
30 h2 = plot(z_freq,z_mag,'.');
31 hold on;
32 h3 = plot(x_freq,x_mag,'.');
33 hold on;
34 h4 = plot(Tz_freq,Tz_mag,'.');
35 hold on;
36 h5 = plot(Ty_freq,Ty_mag,'.');
37 hold on;
38 h6 = plot(Tx_freq,Tx_mag,'.');
39 hold on;
40
41
42 hold off;
43
44 title('Magnitude');
45 xlabel('Frequency [Hz]');
46 ylabel('Magnitude [dB] (0 dB = 1 m)');
47 legend([h3 h1 h2 h6 h5 h4], 'x', 'y', 'z', 'Tx', 'Ty', 'Tz', 'Location', 'southwest');
48 grid on
49 grid minor
50 set(gcf, 'units', 'normalized', 'outerposition', [0 0 0.5 0.6])
51
52 subplot(2,1,2)
53
54
55 plot(y_freq,y_phase,'.');
56 hold on;
57 plot(z_freq,z_phase,'.');
58 hold on;
59 plot(x_freq,x_phase,'.');
60 hold on;
61 plot(Tz_freq,Tz_phase,'.');
62 hold on;
63 plot(Ty_freq,Ty_phase,'.');
64 hold on;
65 plot(Tx_freq,Tx_phase,'.');
66 hold on;
67 hold on;
68
69 hold off;
70
71 title('Phase');
72 xlabel('Frequency [Hz]');
73 ylabel('Phase [ ]');
74 % legend('x', 'y', 'z', 'Tx', 'Ty', 'Tz', 'Location', 'southwest');
75 grid on
76 grid minor
77 set(gcf, 'units', 'normalized', 'outerposition', [0 0 0.5 0.6])
78 print('f_res.eps', '-depsc');
79 movefile('f_res.eps', 'H:\My Drive\12 Bachelor ...
assignment\IDS\Paper\Conference-LaTeX-template_5-8-18\Images');

```

G. Comparison of resonance frequencies with simulation and measurement results

```

1 simulation = [628;173;726;1007;1815;769];
2 measurement = [719;175;676;945;1698;823];
3 calculation = [NaN; 1.745559888444406e+02; 6.343231048450397e+02; 1.098679846006449e+03; NaN; NaN];
4 mode = categorical({'x';'y';'z';'Tx';'Ty';'Tz'});
5 mode = reordercats(mode,{'x';'y';'z';'Tx';'Ty';'Tz'});
6 data = [simulation,measurement,calculation];
7
8 % deviation_sim_meas = (1-(simulation./measurement))*100;
9 % deviation_calc_meas = (1-(calculation./measurement))*100;
10 % deviation = [deviation_sim_meas,deviation_calc_meas];
11
12 % subplot(2,1,1)
13
14 bar(mode,data);
15 % title(' (a) ');
16 xlabel('Mode');
17 ylabel('Resonance frequency [Hz]');
18 legend('Simulation','Measurement','Calculation','location','northwest');
19 grid on
20 grid minor
21
22 % subplot(2,1,2)
23 % bar(mode,deviation);
24 % title(' (b) ');
25 % xlabel('Mode');
26 % ylabel('Deviation [%]');
27 % ylim([-20 20]);
28 % legend('Measurement w.r.t simulation','Measurement w.r.t. calculation','location','southwest');
29 % grid on
30 % grid minor
31 %set(gcf,'units','normalized','outerposition',[0 0 0.4 0.6])
32 print('f_res_comparison.eps','-depsc');
33 movefile('f_res_comparison.eps','H:\My Drive\12 Bachelor ...
assignment\IDS\Paper\Conference-Latex-template_5-8-18\Images');

```

H. Calculation and comparison of the spring constants

```

1 % given constants
2
3 L_0 = 1710e-6; % direct length between starting and end point of beam for compression step ...
0 [m]
4 L_1 = 1695e-6; % direct length between starting and end point of beam for compression step ...
1 [m]
5 L_z = 2230e-6; % approximate length for z-direction (taking compliant base into account)
6 b_th = 50e-6; % theoretical mask width of the beam [m]
7 b_rl = 46e-6; % real width of the beam [m]
8 h = 8.5e-6; % height of the beam [m]
9 E = 169e9; % Young's modulus [GPa]
10 m = 12.7e-6; % weight of the proof mass [kg]
11 F_x = 0.75e-3; % force to compress beam by d = 15 um (according to Jerry)
12 r_Tx = 3350e-6; % r of mass for Tx-mode
13 r_Ty = 1570e-6; % r of mass for Ty-mode
14
15 % calculation of second moment of area
16
17 I_y_th = (b_th*h^3)/(12);
18 I_z_th = (h*b_th^3)/(12); % CAREFUL: B and H are INTERCHANGED because of different moving ...
direction of the springs
19
20 I_y_rl = (b_rl*h^3)/(12);
21 I_z_rl = (h*b_rl^3)/(12);
22
23 % calculation of the spring constant in y-direction without compression
24
25 k_beam_y_0_th = (12*E*I_y_th)/(L_0^3); % spring constant of cantilever beam in y-direction ...
without compression [N/m]
26 k_spring_y_0_th = 4*k_beam_y_0_th;
27 k_tot_y_0_th = 4*k_spring_y_0_th;
28
29 k_beam_y_0_rl = (12*E*I_y_rl)/(L_0^3);
30 k_spring_y_0_rl = 4*k_beam_y_0_rl;

```

```

31 k_tot_y_0_rl = 4*k_spring_y_0_rl;
32
33 f_res_y_0_th = 1/(2*pi)*sqrt(k_tot_y_0_th/m);
34
35 f_res_y_0_rl = 1/(2*pi)*sqrt(k_tot_y_0_rl/m);
36
37 k_y_1_jerry = 1.05;
38 k_y_0_jerry_tot = 16*k_y_1_jerry;
39
40 f_res_y_0_jerry = 1/(2*pi)*sqrt(k_y_0_jerry_tot/m);
41
42 % calculation of the spring constant in y-direction with compression step 1
43
44 k_beam_y_1_th = k_beam_y_0_th - F_x/L_1;          % spring constant of cantilever beam in y-direction ...
45   with compression step 1 [N/m]
46 k_spring_y_1_th = 4*k_beam_y_1_th;
47 k_tot_y_1_th = 4*k_spring_y_1_th;
48
49 k_beam_y_1_rl = k_beam_y_0_rl - F_x/L_1;          % spring constant of cantilever beam in y-direction ...
50   wirl compression step 1 [N/m]
51 k_spring_y_1_rl = 4*k_beam_y_1_rl;
52 k_tot_y_1_rl = 4*k_spring_y_1_rl;
53
54 f_res_y_1_th = 1/(2*pi)*sqrt(k_tot_y_1_th/m);
55 f_res_y_1_rl = 1/(2*pi)*sqrt(k_tot_y_1_rl/m);
56
57 k_y_1_jerry = 0.5;
58 k_y_1_jerry_tot = 16*k_y_1_jerry;
59
60 f_res_y_1_jerry = 1/(2*pi)*sqrt(k_y_1_jerry_tot/m);
61
62 f_calc_th = [f_res_y_0_th; f_res_y_1_th];          % calculated f_res according to theory
63 f_calc_rl = [f_res_y_0_rl; f_res_y_1_rl];
64 %f_calc_jerry = [f_res_y_0_jerry; f_res_y_1_jerry]; % calculated f_res ...
65   according to fig. 20 of Jerry's report
66
67 f_measured_me = [175.47; 127.32];                % measured f_res
68 f_measured_Boris = [184; 125];                    % measured f_res by Boris
69 f_simulation = [173; NaN];
70 compression_step = [0; 15];
71
72 f_data_y = [f_calc_th, f_calc_rl, f_measured_me, f_measured_Boris, f_simulation];
73
74 % calculation of the spring constant in z-direction without compression
75 % (approximately)
76
77 k_beam_z_th = (12*E*I_z_th)/(L_z^3);              % spring constant of cantilever beam in z-direction ...
78   without compression [N/m]
79 k_spring_z_th = 4*k_beam_z_th;
80 k_tot_z_th = 4*k_spring_z_th;
81
82 f_res_z_th = 1/(2*pi)*sqrt(k_tot_z_th/m);
83
84 k_beam_z_rl = (12*E*I_z_rl)/(L_z^3);              % spring constant of cantilever beam in z-direction ...
85   without compression [N/m]
86 k_spring_z_rl = 4*k_beam_z_rl;
87 k_tot_z_rl = 4*k_spring_z_rl;
88
89 f_res_z_rl = 1/(2*pi)*sqrt(k_tot_z_rl/m);
90
91 % calculation of the spring constant in Tx-direction without compression
92 % (approximately)
93
94 k_theta_Tx_th = k_spring_z_th*(r_Tx)^2;
95 J_Tx = (1/3)*m*(r_Tx)^2;
96
97 f_res_Tx_th = (1/(2*pi))*sqrt((4*k_theta_Tx_th)/J_Tx);
98
99 k_theta_Tx_rl = k_spring_z_rl*(r_Tx)^2;
100
101 f_res_Tx_rl = (1/(2*pi))*sqrt((4*k_theta_Tx_rl)/J_Tx);
102
103 % mode = categorical({'x'; 'y'; 'Tz'; 'Tx'; 'Ty'; 'z'});
104 % mode = reordercats(mode, {'x'; 'y'; 'Tz'; 'Tx'; 'Ty'; 'z'});

```

```

100
101 mode = categorical({'Tx';'z'});
102 mode = reordercats(mode,{'Tx';'z'});
103
104 f_data_th = [f_res_Tx_th;f_res_z_th];
105 f_data_rl = [f_res_Tx_rl;f_res_z_rl];
106 f_data_measured = [945.42;675.95];
107 f_data_simulation = [1007;726];
108 f_data_Tx_Ty_z = [f_data_th,f_data_rl,f_data_measured,f_data_simulation];
109
110 %% plot graph y-direction
111 figure
112
113 %subplot(2,1,1)
114 compression_step = [0 15];
115 bar(compression_step,f_data_y);
116
117 % title('Comparison of obtained resonance frequencies in y-direction');
118 % title('a');
119 xlabel('Compression distance [\mum]');
120 ylabel('Resonance frequency [Hz]');
121 legend('Theoretical calculation with b = 50 \mum','Theoretical calculation with b = 46 \mum','My ...
measurement','Earlier measurement','Simulation','location','northeastoutside');
122 grid on;
123 grid minor;
124 %set(gcf,'units','normalized','outerposition',[0 0 0.5 0.6])
125 print('k_y.eps','-depsc');
126 movefile('k_y.eps','H:\My Drive\12 Bachelor ...
assignment\IDS\Paper\Conference-LaTeX-template_5-8-18\Images');
127
128 %subplot(2,1,2)
129 %bar(mode,f_data_Tx_Ty_z);
130
131 % title('Comparison between calculation and measurement (and simulation?)');
132 %title('b');
133 % xlabel('Mode');
134 % ylabel('Resonance frequency [Hz]');
135 % legend('Theoretical calculation with b = 50 \mum','Theoretical calculation with b = 46 \mum','My ...
measurement','Simulation','location','northeast');
136 % grid on;
137 % grid minor;
138 %print('T_x_T_y_z','-dpng');
139
140 %movefile('T_x_T_y_z.png','D:\Google Drive\12 Bachelor ...
assignment\IDS\Paper\Conference-LaTeX-template_5-8-18\Images');

```

APPENDIX D
RAW DATA

All raw data of the measured topographies, modes, videos of the spring compression including burning of the ETAs, SEM images, provided material and documentation on the measurement box are included as an attachment in form of a GDrive link (https://drive.google.com/drive/folders/1ftDI4Q8yRRnIKQ8XNqTiAwE7u_mrHdyZ?usp=sharing) or via the QR-code in Fig. 29.



Fig. 29: QR-code of the Google Drive link for the attachment.